

## Triggering of microearthquakes in Iceland by volatiles released from a dyke intrusion

Hilary R. Martens\* and Robert S. White

*Bullard Laboratories, Department of Earth Sciences, University of Cambridge, Cambridge CB3 0EZ, UK. E-mail: hmartens@gps.caltech.edu*

Accepted 2013 May 4. Received 2013 May 1; in original form 2013 February 7

### SUMMARY

We suggest that carbon dioxide exsolved from a mid-crustal basaltic dyke intrusion in Iceland migrated upwards and triggered shallow seismicity by allowing failure on pre-existing fractures under the relatively low elastic stresses (100–200 kPa; 1–2 bar) generated by the dyke inflation. Intense swarms of microseismicity accompanied magmatic intrusion into a dyke at depths of 13–19 km in the crust of Iceland's Northern Volcanic Rift Zone during 2007–2008. Contemporaneously, a series of small normal earthquakes, probably triggered by elastic stresses imposed by the dyke intrusion, occurred in the uppermost 4 km of crust: fault plane solutions from these are consistent with failure along the extensional fabric and surface fissure directions mapped in the area, suggesting that the faults failed along existing rift zone fabric even though the mid-crustal dyke is highly oblique to it. Several months after the melt froze in the mid-crust and seismicity associated with the intrusion had ceased, an upsurge in shallow microseismicity began in the updip projection of the dyke near the brittle–ductile transition at 6–7 km depth below sea level. This seismicity is caused by failure on right-lateral strike-slip faults, with fault planes orientated  $23 \pm 3^\circ$ , which are identical with the  $24 \pm 2^\circ$  orientation in this area of surface fractures and fissures caused by plate spreading and extension of the volcanic rift zone. However, these earthquakes have *T*-axes approximately aligned with the opening direction of the dyke, and the right-lateral sense of failure is opposite that of regional strike-slip faults. We suggest that the fractures occurred along pre-existing weaknesses generated by the pervasive fabric of the rift zone, but that the dyke opening in the mid-crust beneath it caused right-lateral failure. The seismicity commenced after a temporal delay of several months and has persisted for over 3 yr. We propose that fluids exsolved from the magma in the dyke, primarily carbon dioxide, percolated updip and to shallower depths predominantly along pre-existing fractures. Increased pore pressure from the volatiles reduced the effective normal compressive stress on faults, increasing the likelihood of failure and allowing the modest stress changes generated by the intrusion to cause failure. Propagation of volatiles through the crust would also account for the observed time delay between the intrusion at depth and the shallow earthquake clusters. A further short-lived cluster of earthquakes at 2–4 km depth beneath the surface exhibits left-lateral strike-slip faulting with epicentres well orientated along a lineation which is identical with other subparallel strike-slip faults in the area that transfer motion between two adjacent spreading segments. These shallow earthquakes lie beyond lobes of significant positive Coulomb stress change caused by the intrusion, implying minimal modifications to the stress field in their vicinity; hence, they continue to respond to the regional stress field rather than the local stress field generated by the dyke intrusion.

**Key words:** Fracture and flow; Earthquake interaction, forecasting, and prediction; Volcano seismology; Rheology and friction of fault zones; Dynamics and mechanics of faulting; Volcanic gases.

### INTRODUCTION

Superposition of the mid-Atlantic spreading ridge over a hot mantle upwelling generates Iceland's abnormally thick crust, elevating it above sea level. The spreading centre on Iceland is represented by a

\*Now at: Seismological Laboratory, Division of Geological and Planetary Sciences, California Institute of Technology, Pasadena, CA 91125, USA.

series of seismically and volcanically active neovolcanic rift zones (Einarsson 1991). The Kverkfjöll fissure swarm of the Northern Volcanic Rift Zone in Iceland, where this study is based, is ~10–15 km wide and is characterized by subparallel faults and fissures which cut the recent lava flows (Hjartardóttir & Einarsson 2012). The orientation of the volcanic rift zones and faults are slightly oblique to the plate spreading direction, which here is at an azimuth of 106° (DeMets *et al.* 1994). The work described here is from seismicity accompanying and following melt intrusion in the mid-crust and faulting near Mount Upptyppingar on the edge of the Kverkfjöll segment of the volcanic rift, adjacent to the Askja segment (Fig. 1).

The magma source in the mantle is connected to the crust by a network of dykes, sills and conduits (Key *et al.* 2011a,b; Tarasewicz *et al.* 2012). About three-quarters of the intruded melt freezes in the crust before it is able to erupt at the surface. One such intrusion occurred over a year-long period between 2007 March and 2008 March beneath Mount Upptyppingar in the Kverkfjöll rift segment. Well

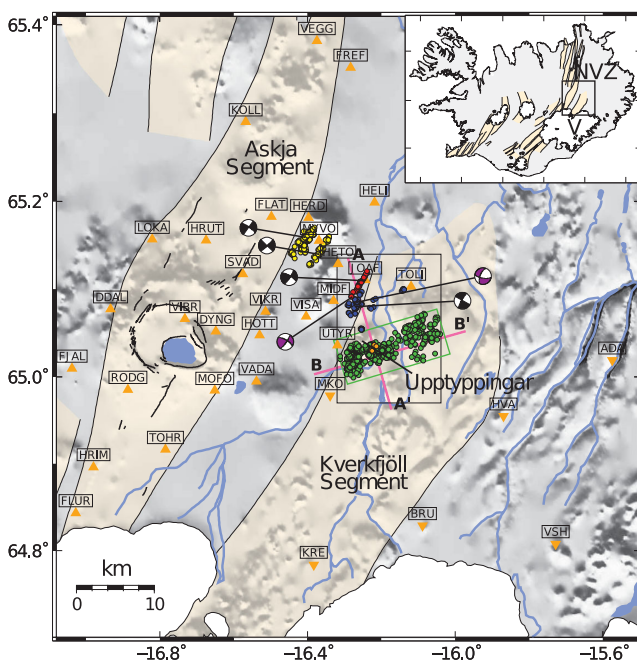


**Figure 1.** Map of the southern section of Iceland's Northern Volcanic Zone (NVZ). Inset shows the whole of Iceland, with the region displayed in the main map outlined by the black box. V marks Vatnajökull ice cap, NVZ the Northern Volcanic Zone. The black box in the main map outlines our study area. Upright orange triangles mark seismic stations deployed by the University of Cambridge; inverted orange triangles show seismic stations maintained by the Icelandic Meteorological Office (IMO). The station HRUT is not shown because it overlaps with the location of station HRUT, and the location of station SVA falls outside the figure bounds. See Table S1 for details of station locations and dates of deployment. Yellow dots are epicentres of regional earthquakes shown for context and comparison. Green, blue and red dots represent deep (> 10 km below sea level), mid-level (5–10 km below sea level) and shallow (< 5 km below sea level) hypocentres, respectively, located using hand-picked *P*- and *S*-wave first arrivals and double-difference relocation. Orange dots represent shallow hypocentres that occurred directly above the deep events, also located using hand-picked arrivals and double-difference relocation. Volcanic segments, including Askja and Kverkfjöll, are depicted by *en echelon*, tan-shaded regions. Characteristic fault plane solutions are provided for the clusters of shallow and mid-level seismic events. Fault plane solutions shaded purple are discussed in greater detail in the text and shown in Fig. 6. Pink lines show the extent and orientation of the two profiles in Fig. 2. The green box approximates the geometry and extent of the dyke, projected onto the surface.

defined by high-frequency (~10 Hz) microseismicity (Jakobsdóttir *et al.* 2008), the melt was injected into a planar dyke dipping southwards at approximately 50° and orientated with a strike direction of 074° (Martens 2010; Martens *et al.* 2010; White *et al.* 2011). The dyke extended in the mid-crust from depths of 19–13 km below sea level, and extended laterally a distance of some 13 km (green box in Fig. 1). It froze before reaching the surface. Analysis of surface deformation observed using Global Positioning System (GPS) measurements and Interferometric Synthetic Aperture Radar (InSAR) data suggest that 42–47 million m<sup>3</sup> of melt was intruded in the dyke (Hooper *et al.* 2011), which attained a maximum thickness of about 1 m in the centre.

The strike of this dyke intrusion is highly oblique to both the plate spreading direction and to the orientation of the neovolcanic rift zones. This unexpected orientation is likely due to perturbation of the local stress field by the rapid melting of Europe's largest ice cap, Vatnajökull, which has occurred in recent years. Unloading of the Vatnajökull ice cap, which lies to the south of Upptyppingar (inset, Fig. 1) causes uplift due to isostatic rebound at a rate measured by GPS of up to 25 mm a<sup>-1</sup> (Arnadóttir *et al.* 2009). This rebound rate is of similar magnitude to the N106°E–N74°W directed extension rate of 20 mm a<sup>-1</sup> caused by plate motions in this region; hence, it may cause the minimum stress direction to rotate. Circumstances are now similar to those when the Icelandic ice caps melted at the end of the last glacial period ~9000 yr ago, although the total isostatic unloading at that time was even greater. That removal of ice load caused a large increase in decompression melt production in the underlying mantle (Jull & McKenzie 1996). A number of nearby eruptive fissures also exhibit orientations similar to that of the Upptyppingar dyke that are highly oblique to the rift trend, such as the 5-km long east–west trending Hrimalda fissure in the Askja rift segment (White *et al.* 2011). Hence, the present dyke may be reoccupying a dyke formed at the end of the last ice age with the same orientation, but which reached the surface at that earlier time. Imposition of a similar stress field as the Vatnajökull ice cap melts at the present day to the stress field at the end of the last ice age makes it favourable both for enhanced melt generation by decompression of the mantle (Hooper *et al.* 2011), and for the melt to intrude at a similar oblique and inclined orientation along a pre-existing structure.

The dyke intrusion at Upptyppingar occurred in the normally ductile region of the crust, well below the brittle–ductile boundary, which locally lies 6–7 km below sea level (Fig. 2; Soosalu *et al.* 2010; Key *et al.* 2011a). As the dyke intruded and froze in the mid-crust it set up new crustal stresses in its vicinity as the propagating melt made space for itself. Characteristics of the deep microseismicity caused by the melt migration and delineating the shape and extent of the dyke are discussed in White *et al.* (2011). Here, we focus on an upsurge in microseismicity shallower than 7 km and updip of the intrusion, which was apparently triggered by the dyke inflation but delayed by several months following the end of the intrusion. A small number of shallow earthquakes also occurred concomitantly with and directly above the inflating dyke: as we show later these are likely caused by elastic stress changes created during the intrusion. Most of the seismicity, however, occurred in the brittle crust updip of the dyke after a temporal gap of several months, and with an aseismic spatial gap from 13 to 7 km below sea level in the ductile crust (Fig. 2).

A deep-seated magmatic intrusion similar to the Upptyppingar dyke occurred within continental lower crust beneath Lake Tahoe in North America from 2003 August–December (Smith *et al.* 2004). A small number of sporadic deep events continued through 2004

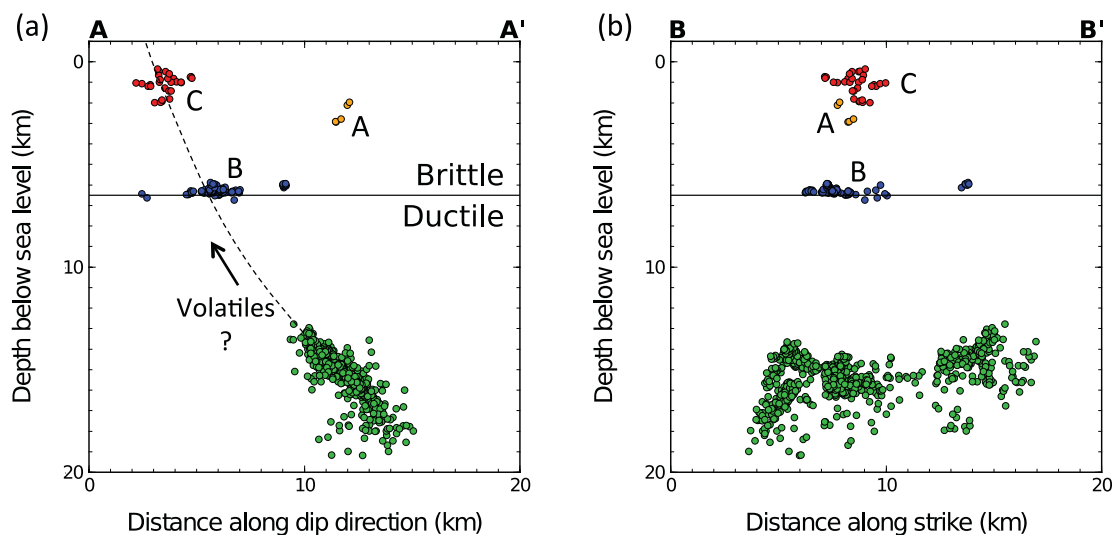


**Figure 2.** Plots of seismicity with depth below sea level taken from profile lines in Fig. 1. Profile A–A' is along the dip direction of the dyke (delineated by the green-coloured hypocentres). Profile B–B' is along the strike direction of the dyke. Hypocentres are coloured and located as described in Fig. 1. The black line at 6.5 km depth denotes the location of the local brittle–ductile boundary inferred from regional seismicity (Soosalu *et al.* 2010; Key *et al.* 2011a,b). The dashed line denotes a hypothetical path for volatiles released by intruded melt to propagate updip of the dyke and towards the surface. See also Movies S1 and S2 in the Supporting Information.

February. High-frequency microearthquakes primarily of magnitude 1–2 delineated the planar geometry of the Tahoe dyke, which propagated and froze within the ductile region of the crust with a dip of approximately  $40^\circ$  (Smith *et al.* 2004; von Seggern *et al.* 2008). Moreover, a notable increase in upper crustal seismicity almost directly above the dyke commenced about 2 months after the start of the intrusion and lasted for over 2 yr (von Seggern *et al.* 2008). Two possible causes of the shallow seismicity have been suggested by von Seggern *et al.* (2008): propagation of volatiles released by the intruding melt or viscoelastic strain accumulation from the deep intrusion leading to positive Coulomb stress changes in the upper crust. We investigate the possibility of these two mechanisms controlling the delayed seismicity we record above the Upptyppingar dyke in Iceland.

Stress changes that enhance shear tractions and reduce the effective normal compressive stress on receiver faults tend to promote failure according to the Coulomb failure criterion (Reasenber & Simpson 1992). Strain accumulation and stress transfer that augment the Coulomb stress on preferentially oriented receiver faults is a generally accepted process by which faults advance in the earthquake cycle (e.g. King *et al.* 1994; Stein *et al.* 1994, 1997; Harris 1998; Freed 2005; Steacy *et al.* 2005). In certain circumstances, the increase in Coulomb stress generated by a large earthquake or a dyke intrusion, for example, might be sufficient to trigger seismic events (Harris *et al.* 1995; Toda *et al.* 2005). Moreover, some evidence exists that even small (subbar) changes in Coulomb stress might be adequate to activate slip on faults that are already close to failure (King *et al.* 1994; Ziv & Rubin 2000; von Seggern *et al.* 2008).

The presence of fluids can further augment the Coulomb stress change on a fault and the likelihood of failure by increasing the local pore fluid pressure and reducing the effective normal compressive stress (e.g. Waite & Smith 2002). Observations of seismic activity interpreted as triggered by the propagation of volatiles, such as carbon dioxide in a gaseous or supercritical fluid state, have been reported elsewhere. Miller *et al.* (2004), for example, postulate that aftershocks following two large earthquakes in northern Italy in 1997 might have been driven by increases in pore fluid pressure caused by

the coseismic release of high-pressure carbon dioxide from a source at depth. Chiodini *et al.* (2004) discuss similar seismic triggering by upward propagating carbon dioxide gas as it accumulates and pressurizes within crustal reservoirs. Shelly & Hill (2011) suggest that rapidly propagating and short-lived seismic swarms beneath Mammoth Mountain could be due to the migration of fluids rich in carbon dioxide. Lindenfeld *et al.* (2012) explore fluid-induced triggering of microearthquakes along the East African Rift. Reyners *et al.* (2007) have also drawn attention to the role of fluids in lower crustal earthquakes near continental rifts.

Many authors have presented observational evidence for seismic triggering by the injection of hydrothermal or magmatic fluids (e.g. Simpson *et al.* 1988; Fournier 1999; Hainzl 2004; Steacy *et al.* 2005; Plateaux *et al.* 2012). If and when the pressure of the injected fluids exceeds the least compressive stress, fractures can dilate. Microseismicity triggered in this context and known as hydraulic fracturing is a widely researched process within the exploration geophysics community (e.g. Grasso 1992; Shapiro *et al.* 1997; Van Eijs *et al.* 2006; Rothert & Shapiro 2007). In addition to reduced effective normal compressive stress and fault dilation, the injection of high-pressure fluids might also trigger seismic events by the forced movement of solidified plugs of melt (White *et al.* 2011) or by generating locally high strain rates (e.g. Fournier 1999; White *et al.* 2011).

In this paper, we model the viscoelastic response of the crust to the Upptyppingar dyke intrusion and compute the Coulomb stress changes on appropriately oriented receiver faults. We show that viscous or elastic stresses imposed by the dyke intrusion are insufficient on their own to cause the time-delayed main sequences of seismicity in the brittle layer. However, we suggest that volatiles, and in particular carbon dioxide released from the intruded magma and propagating up the pre-existing dyke structure, could bring the shallow (<7 km deep) faults to failure by reducing the effective normal compressive stress even with the modest elastic stress changes at these shallow depths that result from the dyke intrusion in the mid-crust. Volatile migration also explains the delay in shallow seismicity as the carbon dioxide released from the melt in the dyke percolated upwards towards the surface. Once a dyke initiates

propagation, it is energetically favourable for it to continue propagating along the same dip direction until a significant change in material properties is reached (Maccaferri *et al.* 2010; White *et al.* 2011). So if the present dyke is reoccupying a dyke formed near the end of the last glacial period, then we might expect the plane of the 2007–2008 dyke intrusion to lie within the earlier dyke intrusion and to extend further updip towards the surface. The shallow seismicity lies approximately on the extension of the present dyke to the surface (Fig. 2), from which we infer that any volatiles triggering the shallow seismicity probably propagated along a structure caused by such a pre-existing dyke.

## EARTHQUAKE LOCATIONS

We use an array of up to 27 three-component seismometers recording at 100 samples per second to investigate the seismicity during the period 2007–2011 within the box shown on Fig. 1 (see Table S1, Supporting Information, for details of the seismometer locations). Six of the seismometers (inverted triangles on Fig. 1) are permanent installations run by the Icelandic Meteorological Office (IMO), mostly with Lennartz (Tubingen, Germany) LE-3D/5s sensors on concrete plinths (Böðvarsson *et al.* 1999). We deployed temporary arrays of up to 21 three-component Guralp (Aldermaston, Berkshire, UK) CMG-6TD broad-band (0.03–50 Hz) seismometers (upright triangles on Fig. 1). These seismometers were mostly buried beneath the surface, which in this region comprises volcanic ash, lava or hyaloclastite, and packed in position with fine sand to provide good coupling to the ground. The seismometer array provides dense coverage around the seismicity, which allows us to determine both good hypocentral locations and well-constrained fault plane solutions.

The Uppþyppingar area of Iceland is remote and seismically quiet. There is little vegetation, very few animals and cultural noise is minimal, with no permanent dwellings. There are no rivers near most of the stations, and the desert conditions mean that the buried sensors remain dry. We recorded earthquakes with local magnitudes down to about  $-1$ , although for our detailed analysis we mostly used earthquakes with magnitudes greater than  $-0.3$  (see Fig. S2).

The 1D velocity model shown in Fig. 3 and Table S2 was used to locate the hypocentres. The velocity model represents a linear interpolation between centre points of a block velocity model derived by Martens (2010). Earthquakes were first located automatically using the Coalescence Microseismic Mapping (CMM) software developed by Drew (2010). We then filtered the automated locations based on modest hypocentre and waveform quality considerations, selecting events that had horizontal location errors better than 1.0 km, vertical location errors better than 2.0 km and signal-to-noise ratios above 2.0. This reduced our catalogue from more than 17 000 microseismic events recorded during our study period to slightly fewer than 5500. Of the *ca.* 5500 higher quality event locations, approximately 2000 were deep events (13–19 km) generated by the movement of magma within the dyke (White *et al.* 2011), another 1500 were shallow events ( $<10$  km) in the Uppþyppingar area (defined by the black box in Fig. 1) and the remaining 2000 were nearby regional shallow events. We henceforth refer to the quality-filtered deep and shallow events in the Uppþyppingar study area as the reduced CMM catalogue.

To aid our interpretation of the spatial distribution and focal mechanisms of the seismicity, we improve location quality further by manually refining the *P*- and *S*-wave arrival times for 170 shallow events, as well as nearly 900 deep events, that had exceptionally clear

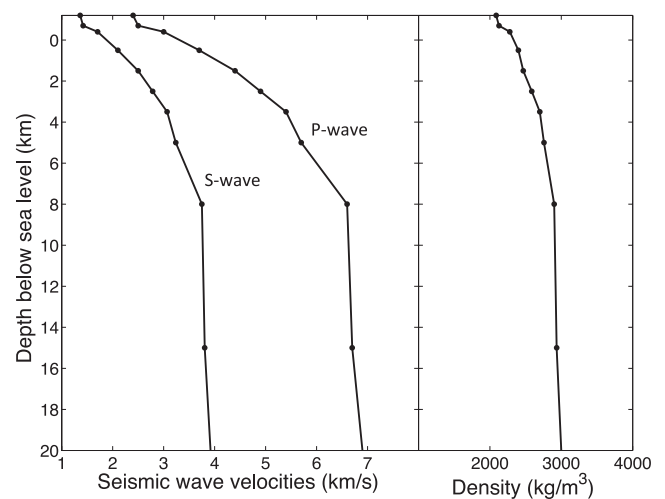


**Figure 3.** Values of seismic wave velocity and density with depth below sea level, used for hypocentre location and finite-element modelling. *P*-wave velocities,  $V_P$ , are derived from a simultaneous inversion for hypocentre locations and a minimum 1D velocity model using VELEST (Kissling *et al.* 1994; Martens 2010). *S*-wave velocities,  $V_S$ , are then computed using a constant  $V_P/V_S$  of 1.76 (Martens *et al.* 2010). Densities are calculated from the seismic velocities using the relationships listed by Darbyshire *et al.* (2000) as appropriate for Iceland.

phase arrivals (signal-to-noise ratios *ca.* 4.5 and above). From the revised seismic wave onsets, we recomputed hypocentral locations using Hypoinverse-2000 (Klein 2002). Hypoinverse-2000 assumes a flat-earth model where the surface layer is defined by the mean elevation of seismic stations near to an event, which is locally about 600 m. Static station correction terms can help to compensate for this assumption of constant elevation. Using CMM-generated look-up tables and a characteristic hypocentre for the shallow clusters, we derived static station correction terms by computing traveltimes differences between the actual elevation of each seismic station and a reference elevation of 600 m. The traveltimes differences at any given seismometer varied only slightly for a variety of source depths that we examined. Since Hypoinverse-2000 also uses the average local surface defined by nearby seismic stations as a zero-depth reference level, we redatum our hypocentres by this amount to obtain depth below sea level. We then further refine the relative locations of our hypocentres using double-difference relocation techniques (Waldhauser & Ellsworth 2000; Waldhauser 2001). This reduces the distortion in locations caused by deviations from the 1D velocity model.

There is a strong correlation between the geometry of the seismic network and the ability to recover the true source depths of seismic events (Tarasewicz *et al.* 2011). This is particularly important for shallow earthquakes such as those we study here. Following the methods of Tarasewicz *et al.* (2011), we performed a number of synthetic tests in which we varied the distance weighting parameters of Hypoinverse-2000. If no distance weighting is applied to the locations, events that are actually shallower than 2 km below sea level are located too deep, by as much as several kilometres for the shallowest events (see Fig. S1). This artefact can be avoided by applying distance weighting to the arrivals so that the arrivals at seismometers close to the epicentre are weighted more heavily than arrivals at more distant stations. Applying full weight to stations within 10 km of a seismic epicentre, zero weight to those beyond 30 km distance and a cosine taper in between yielded the best recovery of depth in our synthetic tests (see Fig. S1). We can recover

the true source depth to within 1 km (and often to better than 100 m) for all of our synthetic hypocentres using this weighting scheme. So this weighting scheme derived from synthetic tests is what we have adopted for the shallow events used in this paper.

The position and shape of the weightings derived from synthetic depth tests will of course change if the network geometry is altered or if time picks are not available from some of the stations. While our network geometry varied slightly over the course of our study period (see Table S1 for details), the recordings at some stations occasionally suffered data gaps, and we are sometimes unable to identify the *P*- and *S*-wave first arrivals on all stations, we estimate that our shallow hypocentre locations are generally within 1–2 km of the true source depth for the shallowest events (<5 km) and within 0.5–1.0 km of the true source depth for the events near the brittle–ductile boundary (5–7 km). The mean double-difference relative relocation error as defined by Waldhauser (2001) is 32 m in depth for all shallow events.

## OBSERVED SEISMICITY

### Hypocentral depths

The dyke intrusion generated over 10 000 recorded micro-earthquakes up to magnitude 2.3 in the mid-crust at depths of 13–19 km between 2007 and 2008 (Jakobsdóttir *et al.* 2008; White *et al.* 2011). We show the best located of those events following manual refinement and double-difference relocations as green symbols on Fig. 2. Movies showing the temporal progression of these events, as well as the shallow seismicity, are included with the Supporting Information (Movies S1 and S2). The cross-sections in Fig. 2 show that the mid-crustal events terminate at a shallowest depth of 13 km. Fault plane solutions from the microearthquakes caused by melt intrusion into the dyke during 2007 July show fault planes aligned at exactly the same dip of 50° as the macroscopic orientation of the dyke delineated by the hypocentres of those events (White *et al.* 2011). This microseismicity is interpreted as caused by the fracture of frozen plugs of melt within the dyke as further intrusions of melt forced their way upwards, or of fracture of the rock immediately adjacent to the dyke. The aligned fault planes may also result from the melt moving up a dyke intruded previously at the end of the last glacial period, and fracturing that previously intruded material. We do not discuss the mid-crustal seismicity further in this paper. For our purposes, the deep seismicity shows the extent and geometry of the dyke intrusion which generated viscoelastic stresses in the crust as the dyke inflated, and thereby stressed the overlying crust.

Fig. 4 depicts the spatial and temporal distribution of all earthquakes from the reduced CMM catalogue that occurred between 2007 January and 2011 May in our study area. The IMO catalogue is used as a supplement to the CMM catalogue for events prior to the deployment of Cambridge University instruments in early 2007 June (prior to day 157). To remain consistent with the filter criteria adopted for the reduced CMM catalogue, we scaled the number of IMO catalogue events by the average ratio of the number of CMM events left after filtering to the original number of events (~1/3). The earthquakes are binned into four clusters based on CMM-determined epicentral location and depth as in Fig. 2. Since CMM does not apply distance weighting to the seismic data, and therefore tends to locate very shallow events too deep (Fig. S1), we redatumed the shallow events based on the average depths of the seismic clusters located using Hypoinverse-2000 with distance weighting. Following the end of the mid-crustal dyke intrusion (marked by deep events coloured green) at the beginning of 2008

April (day 460), there were no further deep events at all. Since the mid-crustal intrusion was in the normally ductile region of the crust, this is not surprising. Indeed the surprising aspect is that there was considerable seismicity associated with the dyke intrusion itself, a fact that we attribute to the locally high strain rates caused by melt movement.

A seismically quiet period lasting 5 months followed the termination of the deep seismicity (day 460) until persistent seismicity (marked by blue events in Fig. 4) started in 2008 August (day 600) near the 6–7 km deep brittle–ductile boundary of the crust. This activity continued for 3 yr through the remainder of the survey. The more or less continuous seismicity and the absence of a main shock suggest that the events are better characterized as a series of seismic swarms than as an aftershock sequence (Hainzl 2004). This deduction is supported by the observation that local magnitudes, published by the IMO, for events in the reduced CMM catalogue remain steady through time and fall primarily between 0 and 1 (Fig. S2; Jakobsdóttir *et al.* 2008). The largest event from the reduced CMM catalogue occurred in the shallow cluster C with a local magnitude of 2.7, over 2 yr after the intrusion began. The second largest event had a local magnitude of 2.3 and occurred in the deep cluster associated with the intrusion. An aseismic spatial gap of 6–7 km separates the shallow events at the brittle–ductile boundary (blue events labelled ‘B’ on Figs 2 and 4) from the deep events triggered directly by the intruding magma at depth (green events).

Nine months later, in 2009 July, a burst of very shallow seismicity (red events labelled ‘C’ on Figs 2 and 4) occurred over a brief 2-week span (days 924–939). Almost all the events in the upper crust occurred directly updip from the dyke and in approximately the same plane as the dyke (broken line on Fig. 2). From this we infer that they are genetically related to a former dyke that extended at least most of the way to the surface. As we discuss later we interpret these shallow earthquakes as triggered by fluids released from melt intruded into the dyke at depth, which then percolated up the former dyke structure towards the surface. The seismicity shallows slightly relative to the planar updip projection of the dyke with greater distance from the intrusion. Furthermore, the shallow seismicity occurs on fractures with different orientations than the dyke, instead apparently reusing existing planes of weakness related to the trend of the rift zone (Fig. 5). Hence, we suggest that the dyke plane may not have extended all the way to the surface, perhaps terminating within the brittle layer, after which the fluids could continue to percolate upwards preferentially along a steeper path. This explains both the location of the overlying seismicity in the brittle crust (Fig. 2) and the time delay from the end of the intrusion.

A handful of events also occurred in the brittle layer (orange events labelled ‘A’ on Figs 2 and 4) during the period of the dyke intrusion itself. Figs 4(c) and (d) show that the events of cluster A immediately follow surges in the deep seismicity. They lie directly above the intrusion (right-hand panel of Fig. 2) and, as we show later, are located off the trend of the dyke and in an area of increased stress caused by the dyke intrusion. We infer that these few small events were caused directly by elastic stress changes generated by the intrusion and were not triggered by fluids. Albeit small and few in number, the fault plane solutions indicate that they fail by normal faulting (Fig. S3a). As discussed later, the *T*-axes are aligned in the direction of spreading and the NNE–SSW orientations of the fault planes are consistent with the regional extensional fabric and the azimuth of surface extensional fissures and fractures (Hjartardóttir & Einarsson 2012).

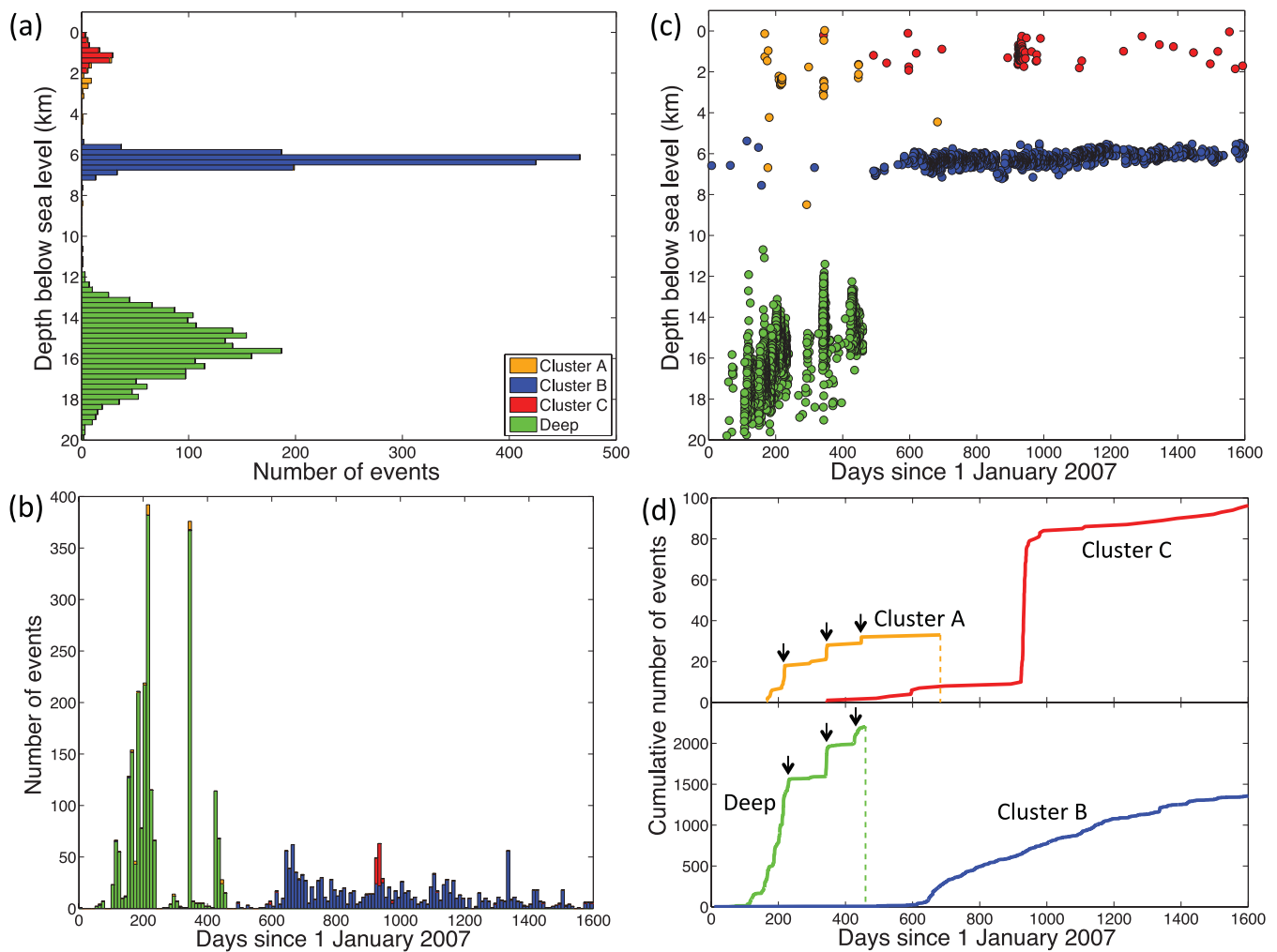


**Figure 4.** Spatial and temporal distributions of hypocentres from the reduced CMM and IMO catalogues (see text for details). Events are coloured by cluster as in Fig. 2. (a) Spatial histogram of hypocentres with depth below sea level in 250-m bins. (b) Time histogram of earthquakes in 10-d bins. (c) Distribution of hypocentres with depth below sea level and through time. (d) Cumulative number of earthquakes through time. The arrows show spikes in shallow seismicity following surges in deep seismicity.

### Epicentral locations

Double-difference relocations were made of the events in the upper crust with the best signal-to-noise ratios. Fig. 5 shows maps of epicentres at the same spatial scale for cluster B at the brittle–ductile boundary (panel a) and for cluster C in the shallow crust (panel b). The mean fault plane solutions of all the events in each cluster are shown inset on the maps and discussed later.

Cluster B continued to be active throughout the 3-yr period of the study from its onset in 2008 August and migrated along strike across the extent of the dyke (Fig. 2b; Movie S2). Earthquakes tended to cluster in swarms, the most prominent of which occurred in 2008 October (light blue colours on Fig. 5a), near the beginning of the seismic activity in the upper crust. There is some evidence of lineation of the epicentres with the same trend as the strike of the rift zone, but it is not pronounced (Fig. 5a).

Cluster C in the shallow crust lasted only 2 weeks, but all the epicentres lay on a single 4-km long lineation orientated  $34 \pm 2^\circ$  (Fig. 5b). This macroscopic lineation of epicentres is indistinguishable from the mean orientation  $38 \pm 6^\circ$  of one of the nodal planes of the strike-slip fault plane solutions calculated from these same 32 events, indicating left-lateral faulting. We do not find much evidence for systematic migration of the epicentres, other than an

observation that events occur more frequently in the central part of the fault and seem to work outwards along the fault over time (see Movie S3).

### Fault plane solutions

We computed double-couple fault plane solutions based on hand-picked polarities of *P*-wave onsets using PPFIT (Reasenber & Oppenheimer 1985). Clear onset polarities were available for almost all the arrivals. The seismometer array provides excellent coverage of the focal sphere for these events, as the lower panels on Fig. 6 demonstrate. We show the fault plane solutions and waveform data for two representative events in Fig. 6 (these are also highlighted in map view on Fig. 1). The event in Fig. 6(a) is from cluster B close to the brittle–ductile boundary; the event shown in Fig. 6(b) is from the shallower cluster C. Both show dominantly strike-slip faulting, but although they occurred only 15 hr apart, they show opposite polarities. Fig. 6(a) shows a right-lateral strike-slip fault; Fig. 6(b) shows a left-lateral strike-slip fault. The raw traces in the upper panels of Fig. 6 show clearly the change in polarities of the waveforms between these two events observed at almost all seismometers. This switch in polarity and in the sense of motion on

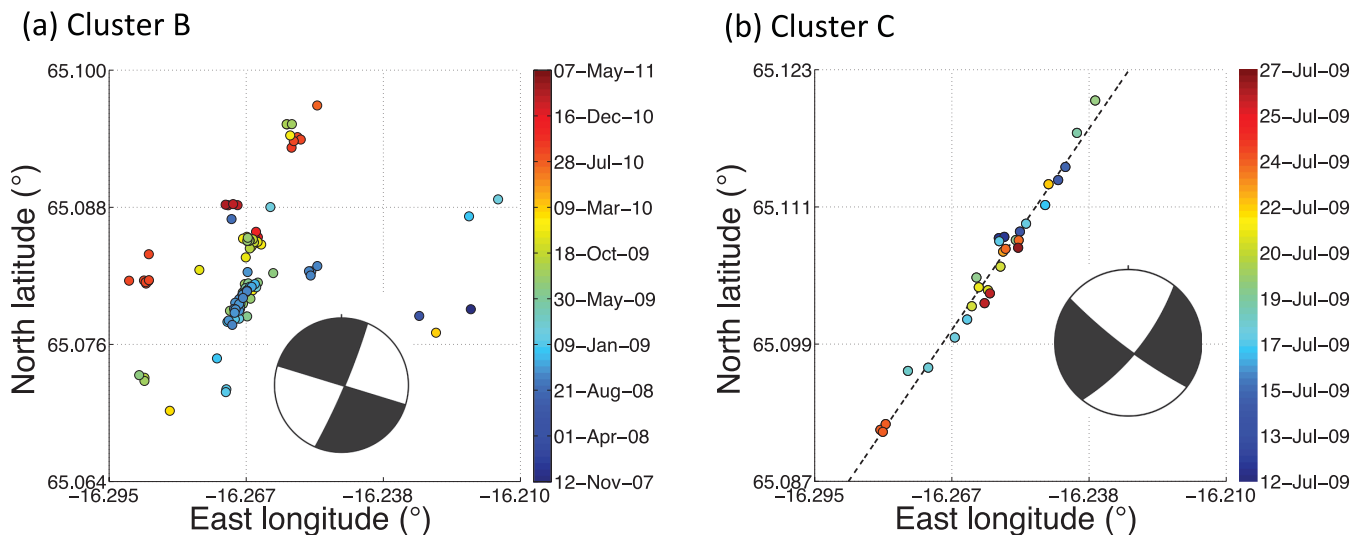


**Figure 5.** Distribution of manually refined epicentres in a Universal Transverse Mercator (UTM) projection for events from (a) cluster B at the brittle–ductile boundary (*ca.* 6.5 km depth b.s.l.) and (b) cluster C at shallow depths (<5 km depth b.s.l.). Epicentres are coloured by event date. Insets show mean fault plane solutions: panel (a) right-lateral strike-slip solutions with mean fault plane strike direction of  $23 \pm 3^\circ$ ; panel (b) left-lateral strike-slip solutions with mean fault plane strike direction of  $38 \pm 6^\circ$ . A linear fit to the epicentres of cluster C, denoted by the dashed line in panel (b), is  $34 \pm 2^\circ$ . See also Movie S3.

the strike-slip faults between clusters B and C is a crucial constraint in the interpretation of the stress modelling we discuss later.

The fault plane solutions from the two events in Fig. 6 are closely representative of all the other events in each cluster. Fault plane solutions from all events in each cluster are shown in Fig. S3. In Fig. 7, we show a compilation of the results. The directions of the nodal planes within each cluster are tightly constrained, and vary little, as the rose diagrams in the upper panels of Fig. 7 demonstrate. Orientations of 1162 fractures cutting the surface in the Upptyppingar region are shown in Fig. 7(c). We conclude that the northeast–southwest trending nodal planes are the fault planes based on the close similarity in directions between the macroscopic lineation of the epicentres (Fig. 5), the surface fractures (Fig. 7c) and the mean directions from the fault plane solutions (Figs 7a and b).

The *T*-axes, the directions of maximum instantaneous strain, are also tightly grouped within clusters B and C (lower panels on Fig. 7), with the *P*-axes (red dots) showing more spread. The mean direction of the *T*-axes for the cluster B events near the brittle–ductile boundary is  $153 \pm 3^\circ$ , which is rotated from the regional spreading direction of  $106^\circ$ , yet almost perpendicular to the  $74^\circ$  strike of the dyke. The good alignment of the *T*-axes with the opening direction of the dyke leads us to suggest that the right-lateral faulting of cluster B is responding to the southeasterly expansion of the dyke as it inflates. By contrast, the mean direction of the *T*-axes for the shallow cluster C events is  $82 \pm 6^\circ$ , suggesting that the left-lateral strike-slip events in this cluster are responding to the approximately east–west regional extensional stress field caused by plate spreading.

The local tectonic structure in the area we are studying is dominated by a series of left-lateral seismically active strike-slip faults spaced  $\sim 3$ – $5$  km apart (Fig. 1), with trends of around  $40^\circ$ . These strike-slip faults take up the extensional motion as it is transferred from the Kverkfjöll segment to the Askja segment (Green 2012). The shallow cluster C events we have mapped follow this structural trend, with the mean fault plane orientation of  $38 \pm 6^\circ$  matching the regional fault trends: as we show below, the cluster C events are in a region that feels very little stress change from the dyke intrusion and so continues to respond to the background regional extension caused by plate spreading and the transfer of spreading between the Kverkfjöll and Askja segments.

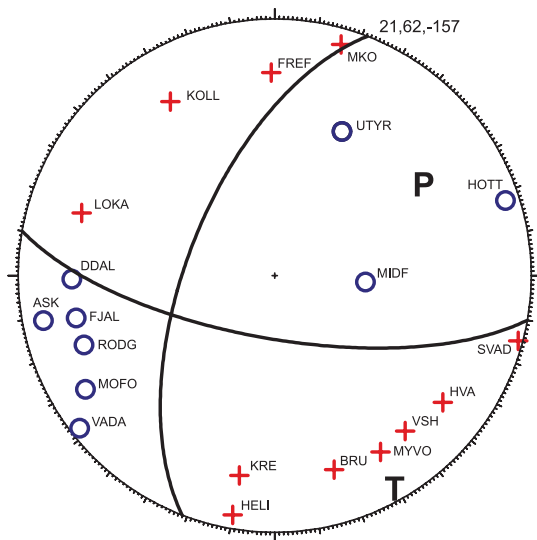
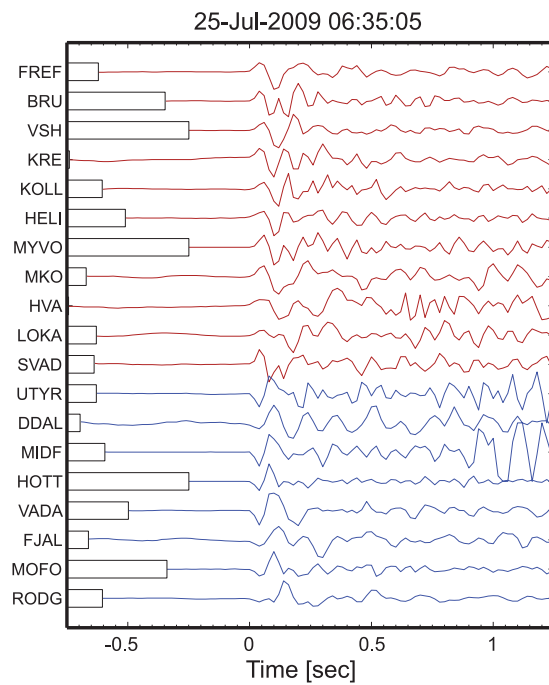
In contrast, the deeper cluster B events at the brittle–ductile boundary exhibit a mean orientation of  $23 \pm 3^\circ$ , which is identical to the mean direction of  $24 \pm 2^\circ$  of 1162 surface fissures and fractures in the Upptyppingar area mapped from satellite and aerial photographs by Hjartardóttir & Einarsson (2012). The surface failures are parallel to the local trend of the rift zone, and probably reflect either direct extension caused by plate spreading, or extension above dykes that themselves are aligned parallel to the rift zone. We suggest therefore that these cluster B faults are reactivating pre-existing fractures or lines of weakness near the brittle–ductile boundary, but that southeasterly extension caused by the inflating Upptyppingar dyke below has caused them to break as right-lateral strike-slip faults. However, the delay in cluster B faulting of several months after the dyke intrusion ended suggests that the elastic stresses imposed by the dyke intrusion were insufficient on their own to cause failure on these faults. It is this observation that leads us to propose that weakening caused by the injection of volatiles released from the injected melt brought the faults to failure, and that the delay represents the time taken for these volatiles to move from the top of the intrusion at 13 km depth to the brittle–ductile boundary at 6–7 km depth. In the next section, we discuss viscoelastic modelling of the dyke intrusion, which allows us to calculate the likely changes in stress in the vicinities of clusters A, B and C.

The cluster A earthquakes were limited in number and in size, but consistently show fault plane solutions with normal faulting (Fig. S3a), with the *T*-axes aligned in the direction of regional spreading and northeast–southwest trending fault planes parallel to the rift zone strike. These few earthquakes are in fact the only ones in our extensive catalogue that show extensional normal faulting, despite being within a rift zone. They also appear to be reactivating existing extensional fabric.

## MODELLING OF STRESS PERTURBATIONS

To investigate the stress changes imposed by the intrusion, we model the influence of an inflating dyke on a surrounding half-space using *Pylith*, a finite element code developed and maintained by the

## (a) Cluster B (brittle-ductile boundary)



## (b) Cluster C (shallow)

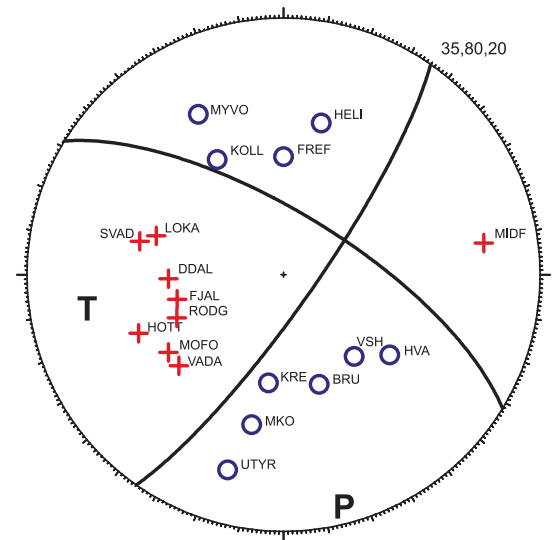
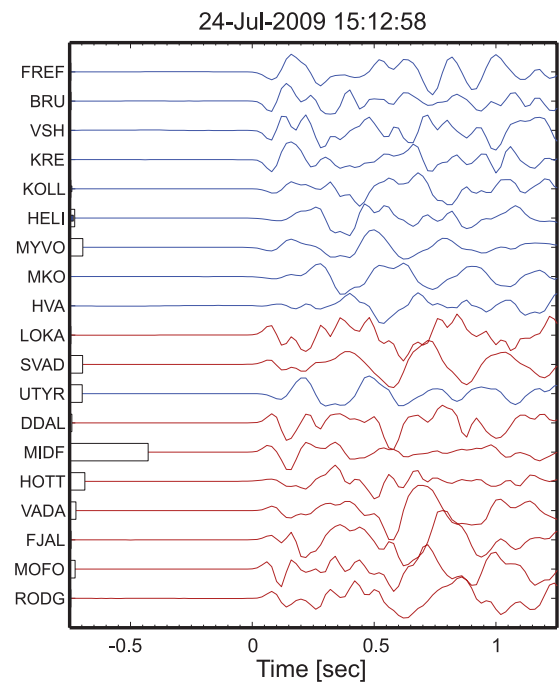


**Figure 6.** Example fault plane solutions from (a) an earthquake 6.6 km below sea level near the brittle–ductile boundary from cluster B; and (b) a shallow earthquake 0.8 km below sea level from cluster C in 2009 July. These events are only 15 hr apart. Top panels show  $P$ -wave arrivals on vertical component traces, with amplitude normalized and bandpass filtered 2–20 Hz: red traces show compressional first arrivals, blue traces show tensional first arrivals. Scale bars at the left-hand side of each panel show absolute amplitudes of  $P$ -wave arrivals used to normalize traces. Note that the shallow event in (b) is much smaller in magnitude than the brittle–ductile boundary event in (a), although the signal-to-noise ratio remains good. Lower panels show fault plane solutions: note the good coverage of the focal sphere and the opposite polarities of the strike-slip faulting and the waveform traces between (a) and (b). The fault plane solutions presented here appear in Fig. 1 as the purple-shaded ‘beach balls’.

Computational Infrastructure for Geodynamics (CIG) community to examine crustal deformation processes (Williams *et al.* 2005; Aagaard *et al.* 2008). Our modelled dyke extends from 13 to 19 km depth below sea level with a dip of  $50^\circ$ . We apply 1 m of tensile opening at the centre of the dyke (0.5 m on each side of the centre line), and taper to zero displacement at the edges, as detailed in

Table S3 and shown in Fig. 8. We also add 0.5 m of left-lateral slip between the dyke walls to match more precisely geodetic observations at the surface (Hooper *et al.* 2011; Fig. 8; Table S4). All displacements applied to the dyke walls are assumed to occur instantaneously. We justify this assumption by noting that the Maxwell relaxation time of the material surrounding the dyke is



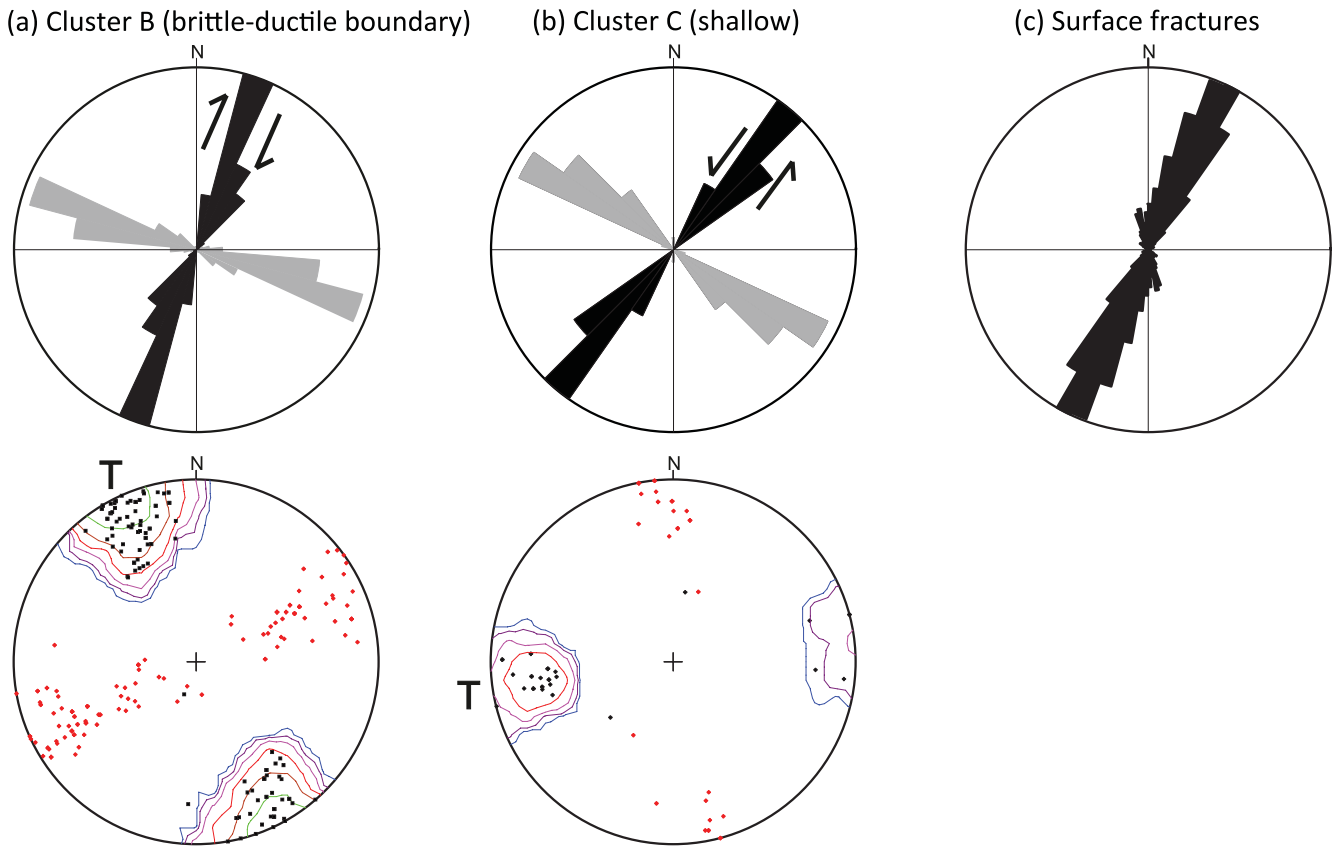


**Figure 7.** Summary of results from fault plane solutions made using FPFIT (Reasenber & Oppenheimer 1985) for (a) 128 earthquakes from cluster B near the brittle–ductile boundary at *ca.* 6–7 km below sea level, and (b) 32 earthquakes in the cluster C swarm during 2009 July at *ca.* 0–2 km below sea level. Top row shows rose diagrams of the directions of the inferred fault planes (black) and auxiliary planes (grey), with sense of motion on faults shown by arrows. Mean direction of fault planes from cluster B is  $23 \pm 3^\circ$ , and from cluster C is  $38 \pm 6^\circ$ . Bottom diagram shows equal area lower hemisphere projection of the azimuths and dips of *T*-axes (black dots) and *P*-axes (red dots) from all fault plane solutions. *T*-axes are contoured with successive intervals doubled: 2, 4, 8, 16, 32, 64 per cent. The mean direction of *T*-axes from cluster B is  $154 \pm 3^\circ$ , and from cluster C is  $82 \pm 6^\circ$ . (c) Directions of 1162 surface fractures in the Uppptyppingar area mapped from satellite and aerial photographs by Hjartardóttir & Einarsson (2012), showing a mean direction of  $24 \pm 2^\circ$ .

*ca.* 1000 yr (Hooper *et al.* 2011) whereas the expansion of the dyke occurred over a much shorter time period of just 1 yr. The elastic and viscous responses of the model space to the intrusion are determined using a quasi-static formulation of the elasticity equation; time-dependent effects arise only from specified constitutive relations.

Our model space consists of a volume 100 km along dip by 100 km along strike by 40.6 km in depth (0.6 km above sea level and 40 km below), discretized into hexagonal elements  $\sim 500$  m on each side. The brittle–ductile boundary is set at 6.5 km depth below sea level. An elastic material model defines the brittle region above 6.5 km and a Maxwell viscoelastic material model defines the ductile region below 6.5 km. The spatial database for the material models is provided in Table S2. For the viscoelastic region, we applied a constant viscosity of  $1.3 \times 10^{21}$  Pa s, as inferred for the lower crust beneath Uppptyppingar by Hooper *et al.* (2011). Boundary conditions constrain the exterior of the grid, prohibiting displacements normal to each edge and disallowing rigid body rotation. The surface, however, remains traction free and unconstrained. Our models neglect the influence of external stress regimes and body forces, such as regional spreading and gravity, respectively.

We set the tolerance for solution convergence at  $1.0 \times 10^{-8}$  for a relative decrease in the residual norm and at  $1.0 \times 10^{-12}$  for an absolute value of the residual norm. We considered a fulfilment of either tolerance sufficient for convergence. The elastic solution

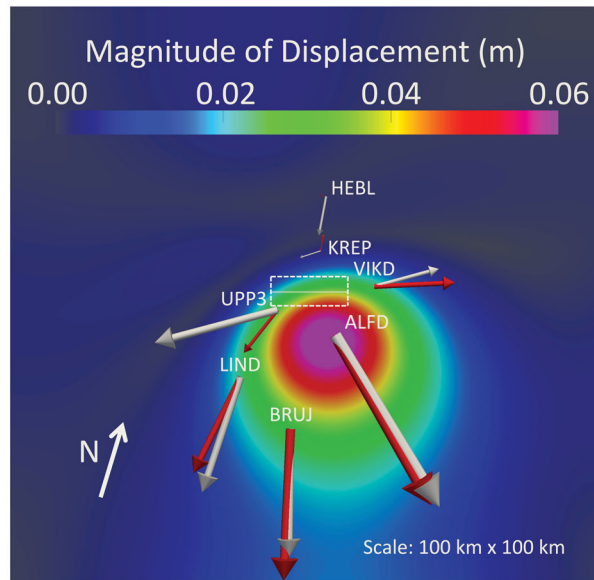
converged to the relative tolerance after 562 iterations, with an absolute residual norm of  $4.5 \times 10^{-10}$ . Additional solutions probing the viscous effects of the intrusion, arising from the viscoelastic constitutive relation we stipulated for the lower crust, were computed for a time period of 200 d in 10-d increments. 200 d represents the approximate amount of time between the termination of the intrusion and the commencement of the shallow swarms. The time-dependent solutions converged by absolute tolerance after about 230 iterations.

Every solution contains a stress tensor for each element in the mesh. To compute the Coulomb stress change, we first rotate each stress tensor to the orientation of our preferred receiver faults: 24/65/–90, 23/90/180 and 38/90/000, representing the mean strike/dip/rake (in degrees) for clusters A, B and C, respectively. The rake is  $0^\circ$  for left-lateral strike-slip faults,  $-90^\circ$  for pure normal faults,  $180^\circ$  for right-lateral strike-slip faults and  $90^\circ$  for pure thrust faults. Strike is measured clockwise from north and dip is measured in degrees between the fault plane and the surface horizontal.

Using the rotated stress tensors, we determine normal and shear tractions on the receiver fault plane and compute the Coulomb stress change. Neglecting changes in pore pressure and cohesion, Coulomb stress change may be written mathematically as

$$\Delta\sigma_f = \Delta\tau_s - \mu\Delta\sigma_n, \quad (1)$$

## (a) Map view



## (b) Depth profile

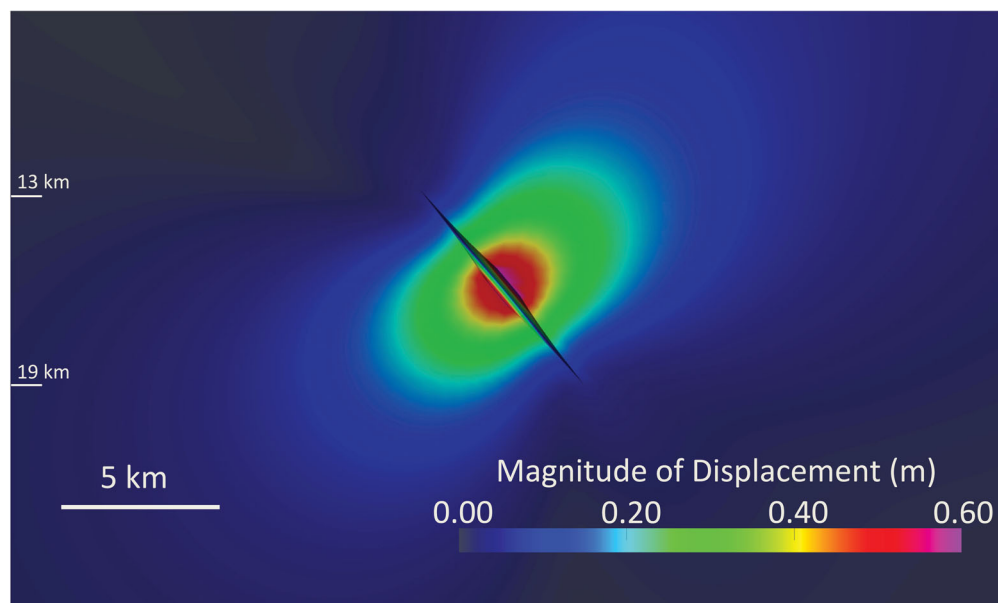


**Figure 8.** (a) Magnitude of 3D surface displacements due to the elastic opening and translational motion of the dyke. The arrows depict observed (beige) and modelled (red) horizontal displacement vectors at the locations of seven GPS stations that recorded the intrusion (Hooper *et al.* 2011). The GPS displacement arrows are exaggerated by a factor of  $9 \times 10^5$ . Exact values of the modelled displacements in all three spatial directions are listed in Table S4. Observed GPS displacements are also provided in Table S4 for comparison. The grey bar in the centre represents the vertical upward projection of the centre of the dyke; the dashed line outlines the vertical upward projection of the extent of the inclined dyke. (b) A slice along the dip direction of the dyke and looking along strike, showing the magnitude of 3D spatial displacements imposed by our modelled dyke (see text for details). Displacements in the mesh elements have been exaggerated by a factor of 500.

where  $\Delta\sigma_n$  is the change in normal tractions on the receiver fault (positive in compression),  $\mu$  is the effective coefficient of friction,  $\Delta\tau_s$  is the change in shear stress on the receiver fault (positive for shear directed along the receiver fault rake) and  $\Delta\sigma_f$  is the change in Coulomb stress on the receiver fault (Reasenber & Simpson 1992; King *et al.* 1994; Toda *et al.* 2005). The effective coefficient of friction assumes that changes in pore fluid pressure are proportional to changes in the normal stress (e.g. Freed 2005); this assumption

is independent of any external injection of fluids. We assume a constant effective friction coefficient of 0.4 for all our calculations. Seismic failure is promoted when a receiver fault experiences a positive change in Coulomb stress. As we show later, the Coulomb stress change at the shallow depths of cluster C, which lies furthest from the dyke, is very small. The receiver faults of clusters A and B, however, experience significant and positive Coulomb stress change due to the dyke inflation.

### Elastic response

Fig. 9 (left-hand panels) shows the elastic response of the crust to instantaneous dyke expansion as the distribution of Coulomb stress change resolved on receiver faults representative of cluster B: right-lateral strike-slip faults striking  $23^\circ$ . Cluster B lies within a lobe of positive Coulomb stress change, reaching levels of 100–200 kPa (1–2 bar) at the brittle–ductile boundary where the events cluster. This suggests that the elastic stresses produced by dyke expansion would tend to promote failure on the right-lateral receiver faults of cluster B.

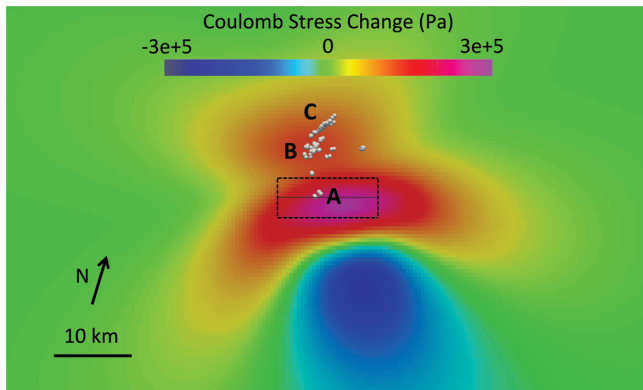
Although cluster A also lies within a lobe of positive Coulomb stress change for right-lateral receiver faults, a more applicable receiver fault geometry for cluster A might be a normal fault dipping eastwards as a result of regional extension (Fig. S3a). The fault plane solutions for cluster A are not well constrained, but the mean strike of the nodal planes is consistent with the regional rift trend; hence, we opted for a simple normal fault geometry with this orientation. We cannot differentiate with certainty, however, which nodal plane is the fault plane. Fig. 10 (left-hand panels) shows the Coulomb stress

change for normal faults striking at  $24^\circ$  and dipping eastward at  $65^\circ$ ; Fig. S4 (left-hand panels) shows the Coulomb stress change for normal faults of the same orientation dipping westwards at  $25^\circ$ . The Coulomb stress change at the location of cluster A is much larger for the receiver fault geometry shown in Fig. 10; hence, if the events were elastically triggered by the dyke, then it is likely they failed along faults dipping towards the east. The positive Coulomb stress change of 100–200 kPa (1–2 bar) around cluster A corroborates our hypothesis that the events were triggered elastically in response to the dyke inflation. Indeed, other studies have found that even subbar stress changes are sufficient to cause failure (King *et al.* 1994; Ziv & Rubin 2000; von Seggern *et al.* 2008). Furthermore, spikes in the number of cluster A events occurred immediately following surges in deep seismicity triggered directly by the intruding melt (Fig. 4d) which suggests that they are directly caused by stress changes generated by the dyke intrusion.

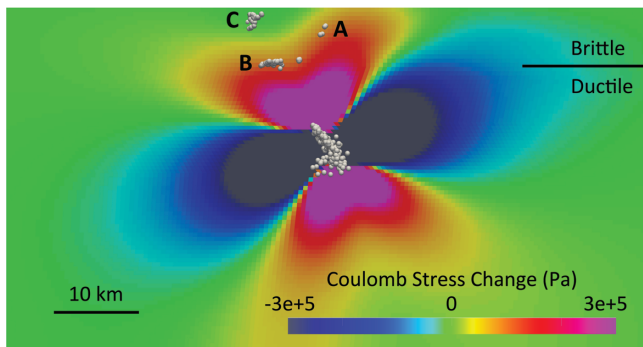
As depicted in Fig. 10 (right-hand panels), we also explored the stress changes resolved on left-lateral strike-slip receiver faults orientated along the mean strike direction for cluster C of  $38^\circ$  (Fig. 5b). We note that the expanding dyke has a minimal to negligible effect

### Elastic Response: Cluster B (023/90/180)

(a) Map view: 6.5 km depth below sea level

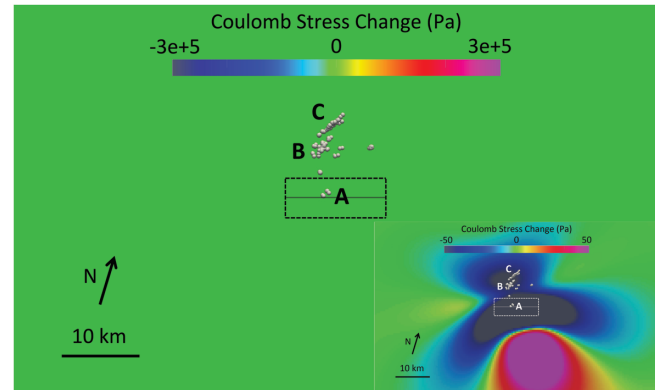


(b) Depth profile



### Viscous Response: Cluster B (023/90/180)

(c) Map view: 6.5 km depth below sea level



(d) Depth profile

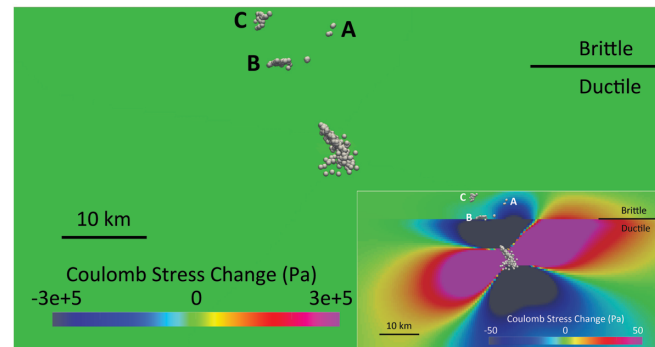


**Figure 9.** Coulomb stress change on right-lateral strike-slip receiver faults oriented  $23/90^\circ$  at the brittle–ductile boundary (6.5 km below sea level). The left-hand panels (a and b) depict Coulomb stress changes based on a purely elastic response to instantaneous dyke opening and slip. The right-hand panels (c and d) represent Coulomb stress changes based on the viscous response after a period of 200 d following instantaneous dyke opening. The upper layer in the viscous model is isotropic elastic; the lower layer is Maxwell viscoelastic with a constant viscosity of  $1.3 \times 10^{21}$  Pa s (Hooper *et al.* 2011). We assume a constant effective friction coefficient of 0.4 and neglect external changes in pore pressure. Densities and seismic wave velocities adopted for our model are listed in Table S2. Panels (a) and (c): Map view. The grey line in the centre of the figure delineates the upward projection of the dyke at its central depth (16 km); the dashed black line outlines the vertical upward projection of the extent of the inclined dyke. The dyke is 13 km in lateral extent, tapering to the edges, and aligned with the horizontal axis of each figure. Geographic north is  $16^\circ$  clockwise from the vertical axis of the figure. Beige points represent hypocentre locations of earthquakes shallower than 6.5 km depth. Panels (b) and (d): Depth profiles cutting through the centre of the dyke along its dip direction. Beige points depict earthquake hypocentres. The deep hypocentres (13–19 km depth) delineate the dyke. The spatial scale bar applies to both horizontal and vertical directions.

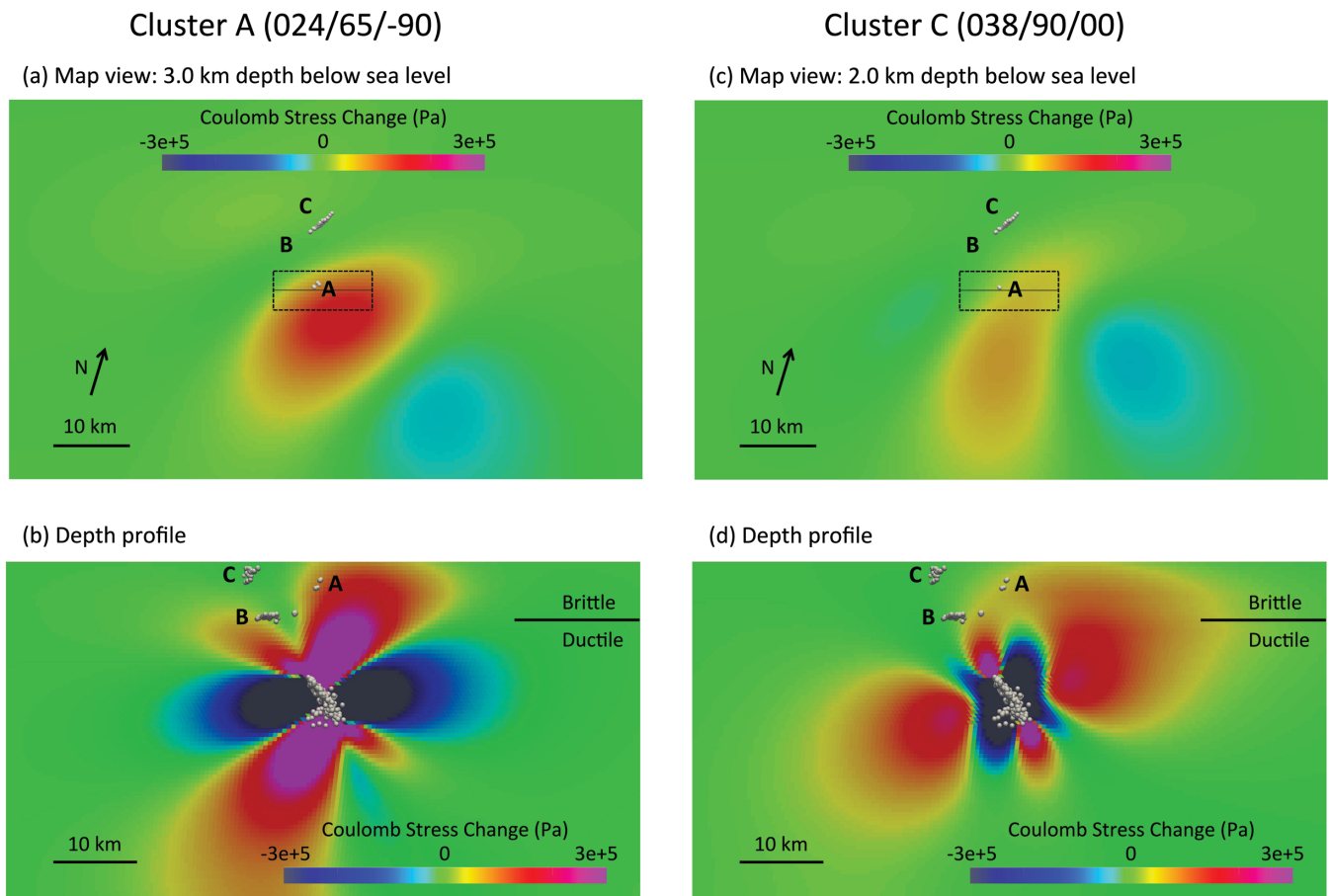


**Figure 10.** Coulomb stress change on receiver faults representative of cluster A (left-hand panels) and cluster C (right-hand panels). For cluster A, we compute the Coulomb stress change on receiver faults orientated 24/65/–90. For cluster C, we compute the Coulomb stress change on receiver faults orientated 38/90/000. Densities and seismic wave velocities adopted for our model are listed in Table S2; the effective coefficient of friction is 0.4. Panels (a) and (c): Map view at 3 and 2 km depth, respectively. The grey line and the dashed black line define the dyke extent and geometry as described in Fig. 9. Beige points represent hypocentre locations, also as in Fig. 9. Panels (b) and (d): Depth profiles cutting through the centre of the dyke along its dip direction.

on the events of cluster C. Cluster C straddles a boundary between positive and negative Coulomb stress change, with no events experiencing a stress change magnitude greater than  $\sim 1$  kPa (0.01 bar). Left-lateral strike-slip faults aligned with the regional rift trend are also either minimally affected by the dyke intrusion or are even brought further from failure (Fig. S4, right-hand panels).

### Viscous response

To examine the effect of viscous relaxation, we subtract the elastic response from the final time step of our model (200 d) and recompute the Coulomb stress change for receiver faults representative of cluster B. The time-dependent stress changes result from the Maxwell viscoelastic material in the lower crust of our model. We implement strain as a step function at the initial time step to simulate the maximum displacements imposed by the dyke before the melt apparently froze and the dyke stopped inflating. We then monitor the relaxation of the stress field through time. As shown in Fig. 9 (right-hand panels), the pattern of positive and negative Coulomb stress changes for the viscous response is opposite that of the purely elastic response. Hence, regions brought closer to failure by the initial intrusion begin to lock over time. The magnitude of Coulomb stress change due to the viscous response, however, is extremely small:  $-50$  to  $30$  Pa ( $-0.0005$  to  $0.0003$  bar) at the brittle–ductile transition after 200 d. Hence, we conclude that the dominant fac-

tor controlling the local stress field as a result of the intrusion is the elastic response. The viscous response has only a very minor, indeed negligible effect. Results are analogous for receiver faults representative of clusters A and C as well, since stress changes due to the viscous relaxation alone are so small.

The magnitude of the lower crustal viscosity alters the magnitude of the stress change. Smaller viscosities correspond to a reduction in the Maxwell relaxation time of a material, thereby increasing the magnitude of stress change due to viscous relaxation over a given time period. The models depicted in Fig. 9 (right-hand panels) assume a viscosity of  $1.3 \times 10^{21}$  Pa s, though lower values are also justifiable. Pollitz & Sacks (1996) derived a viscosity of  $3 \times 10^{19}$  Pa s for the lower crust beneath northeast Iceland using campaign GPS data. Using this viscosity and a right-lateral strike-slip receiver fault orientated at an azimuth of  $23^\circ$ , the magnitude of Coulomb stress change due to the viscous response is still less than 2 kPa (0.02 bar) and indicates locking. Even with the reduced viscosity, the elastic response remains dominant over the viscous response by more than two orders of magnitude.

### DISCUSSION

The intrusion of magma into the Uppþyppingar dyke was both accompanied by and followed by microseismic swarms at shallow depths. Shallow events coincident with the intrusion occurred

sporadically and several kilometres directly overhead of the dyke (cluster A). Fault plane solutions for these events are not well constrained, but six of the highest quality events suggest normal faulting with orientations consistent with having been generated in response to the dyke opening, but reusing the rift-parallel fabric. Extension at the surface with the same orientation was also produced during the Uppþyppingar dyke intrusion (see fig. 9c of Hjartardóttir & Einarsson 2012). We propose that the strain imposed by the inflating dyke increased the Coulomb stress on normal faults aligned with the regional rift fabric, bringing some of them to failure. Our elastic stress models (Fig. 10) corroborate this hypothesis. Furthermore, spikes in the frequency of the cluster A events occur immediately following sharp increases in the rate of deep seismic events associated with melt migration in the dyke (Fig. 4d).

Several months after the cessation of the mid-crustal intrusion, additional swarms of shallow microseismicity commenced above and updip of the dyke in the brittle layer of the crust. A majority of the upsurge in shallow seismicity occurred just above the brittle–ductile transition and persisted for over 3 yr (cluster B). A second seismic swarm broke out even further updip along the extension of the dyke at very shallow depths and more than 1 yr after the intrusion ceased, primarily during a 2-week period in 2009 July (cluster C).

Fault plane solutions for the seismicity in both clusters B and C exhibit strike-slip motion. The sense of slip for the two clusters, however, is opposite one another: right-lateral for the brittle–ductile boundary events of cluster B and left-lateral for the shallower events of cluster C. The spatial and temporal proximity of the cluster B and C events, which exhibit opposite senses of slip, provide constraints on the state of local stress, and allow us to deduce that the maximum deviatoric stress required to trigger the cluster B events is only 200 kPa (2.0 bar) in the presence of fluids.

As depicted in Fig. 7, the mean fault plane direction for cluster B is  $23^\circ$ , identical to the trend of the rift zone and the orientations of extension fractures and fissures at the surface. The mean  $T$ -axis azimuth of cluster B events is  $153 \pm 3^\circ$ , close to the tensile opening direction of the dyke of  $164^\circ$ . We infer that the right-lateral motion on all cluster B strike-slip faults is responding to a modified local stress field set up by the dyke.

The mean fault plane direction for cluster C is  $38^\circ$ , nearly identical to the azimuth of other clusters of lineated left-lateral strike-slip faults that lie west of our area (Green 2012). The average  $T$ -axis azimuth for cluster C is  $82 \pm 6^\circ$ , which is indistinguishable within error from the  $T$ -axis directions of the other regional strike-slip faults (Fig. 1). We infer that the left-lateral motion on all the cluster C strike-slip faults is responding to the local mid-Atlantic ridge spreading direction of  $106^\circ$  and the transfer of motion between spreading segments (Fig. 11 and Green, personal communication, 2013).

Models of elastic crustal deformation resulting from the Uppþyppingar dyke inflation suggest that cluster B near the brittle–ductile boundary lies within a lobe of positive Coulomb stress change for right-lateral strike-slip receiver faults orientated at  $23^\circ$  (Fig. 9). Cluster C nearer the surface lies within a region of minimal Coulomb stress change for receiver faults of the same orientation. For left-lateral receiver faults aligned with regional transfer faults at  $38^\circ$  or with the rift fabric at  $23^\circ$ , the region surrounding cluster C is minimally affected and the elastic modelling shows that the region surrounding cluster B is either minimally affected or becomes locked (Fig. 10 and Fig. S4).

We postulate that the dyke intrusion modified the local stress field, rotating the local stress tensor and bringing the regions containing clusters A and B closer to failure. Fig. 11 summarizes the driving forces behind the faulting types characteristic of clusters A, B and C: for cluster A, normal faulting consistent with extension of the rift, but perhaps triggered in response to the dyke inflation; for cluster B, right-lateral strike-slip faulting aligned with the regional rift fabric, but failing in a direction consistent with the dyke inflation and for cluster C, left-lateral strike-slip faulting consistent with a transfer of extensional motion between rift segments. Our seismic observations and Coulomb stress models suggest that the elastic response of the crust to the inflating dyke was apparently sufficient to trigger the cluster A events outright, particularly following large bursts in deep seismicity that accompanied rapid injections of melt (White *et al.* 2011; Fig. 4d). The initiation of clusters B and C, however, occurred several months after the deep seismicity terminated; hence, although dyke expansion might have advanced the cluster B faults towards

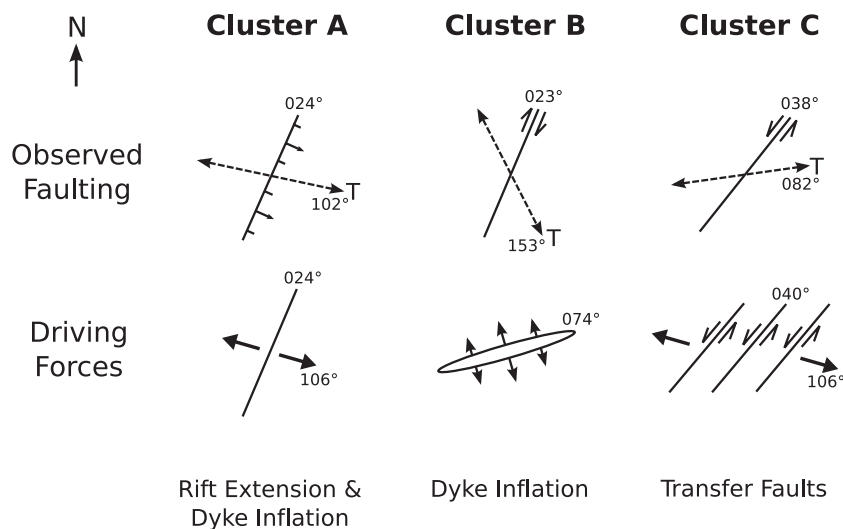


**Figure 11.** Cartoon diagram of the observed mean  $T$ -axis and fault plane directions for clusters A (left), B (middle) and C (right). The lower panel shows the dominant driving forces contributing to the observed fault patterns: tectonic extension and dyke inflation (cluster A), dyke inflation (cluster B) and the transfer of tectonic extensional stress between rift segments (cluster C). The normal faults of cluster A could be either east or west dipping, but our elastic stress models suggest that east dipping is more likely.

failure, imposed elastic stress changes alone were not sufficient to trigger the events. We also note that GPS recordings of velocities at the surface return to background rates immediately following the intrusion, providing no evidence for subsequent aseismic slip (Hooper *et al.* 2011).

Instead, we propose that volatiles, released from magma in the dyke, propagated updip along a pre-existing fracture system created by an earlier generation of dyke intrusion and triggered the time-delayed shallow seismicity near the brittle–ductile boundary (cluster B) by reducing the effective normal compressive stress. Increased pore fluid pressure reduces the effective normal compressive stress at a fault interface, thereby increasing the Coulomb stress and bringing a fault closer to failure. Studies have shown that pore pressures of only 2–3 bar can be sufficient to trigger seismic events (Kisslinger 1976). The events of cluster C might also have been triggered this way, since they occurred several months after the cluster B swarms initiated and lay even further updip of the dyke. Beyond the reach of significant Coulomb stress change, the cluster C faults could have advanced due to the injection of volatiles but failed in a sense consistent with regional extension. For completeness, we acknowledge that the cluster C events might also have failed in response to regional tectonic stresses alone, and that the apparent spatial and temporal connection to the intrusion might simply be a coincidence.

The opposite sense of contemporaneous strike-slip failure between right-lateral cluster B events near the brittle–ductile boundary and left-lateral cluster C events in the shallow upper crust allows us to place constraints on the stress change necessary to cause the cluster B faulting. The stress modelling shows that the shallow cluster C events are minimally affected by the change of stress caused by the intrusion, so are responding to the regional stress field caused by plate separation in the same way as several other nearby parallel strike-slip faults. The normal presumption would be that the deeper cluster B events near the base of the brittle layer would fail in the same way, as left-lateral strike-slip faults. The observation that their polarity is reversed, to become right-lateral faults, suggests that the additional stresses imposed by the dyke intrusion are sufficient both to overcome any pre-existing stresses that would cause left-lateral faulting, and then to cause the observed right-lateral faulting.

If our Coulomb modelling is correct, then the additional 200 kPa (2.0 bar) of Coulomb stress the dyke intrusion produces on the cluster B faults is sufficient to cause failure in this opposite sense, most likely aided by the presence of fluids. This is a small stress change, and represents the maximum stress change required for failure, since part of it might be used to overcome any pre-existing local deviatoric stresses. Hence, we infer that the cluster B events occurred at a depth that accommodates brittle failure, yet lacks a significant build-up of deviatoric tectonic stress, which we assume must have been close to zero at the time of the faulting. This situation could occur at the transition between the base of the brittle crust and the top of the ductile crust, below which stresses are relieved primarily by ductile flow and above which stresses are relieved by brittle failure.

Deviatoric stresses generally increase with depth from the surface through the brittle layer due to the increase in overburden pressure. However, as the depth continues to increase, so does the temperature, until eventually the material becomes weaker as the temperature rises. Below the brittle–ductile transition, the homologous temperature is sufficiently high to allow the deviatoric stress to be relieved through ductile flow under normal tectonic stresses. We suggest that the cluster B events occur right at the brittle–ductile transition where deviatoric stresses are very low. This inference is

corroborated by the observation that the faulting is restricted to a narrow depth band (Fig. 4). From this, we infer that the overlying brittle layer contained enough deviatoric stress (favouring the regional left-lateral faulting) to prevent the right-lateral cluster B events from propagating any shallower, given the maximum 200 kPa driving stress change. Furthermore, since the depth to which brittle failure can be accommodated is governed both by the temperature and the strain rate, this raises the possibility that the inferred migrating fluids allowed sufficiently high strain rates to cause brittle failure slightly deeper than the normally brittle zone and within the uppermost section of the normally ductile layer. We also note that the Coulomb modelling shows that the dyke-induced stress changes decrease rapidly towards the surface (Fig. 9b), so as they dropped below 200 kPa they may anyway have been insufficient to cause faulting.

Since the shallow events occur along faults orientated at similar azimuths to surface fractures (Fig. 7), we suggest that the extension of the dyke plane extended only partially towards the surface, perhaps nearing the brittle–ductile interface. The pre-existing fault structure could provide a pathway of least resistance to the volatiles. At the upward extent of the pre-existing fault structure, buoyancy forces would encourage the volatiles to percolate upwards more directly. Our observation that the shallow seismicity lies slightly above the updip projection of the intrusion is consistent with this claim (Fig. 2). Alternatively, the pre-existing fault structure might extend all the way to the surface and steepen as it approaches the surface.

The most likely culprit for volatiles released from basaltic magmas in the Upptyppingar intrusion is carbon dioxide. Although water, sulphur dioxide and other volatiles are likely to be present, they are at lower concentrations and remain dissolved in the magma until shallower depths. In contrast, carbon dioxide starts to exsolve from rising magmas at depths of 15–20 km as they decompress and become supersaturated (Pan *et al.* 1991; Lowenstern 2001). Crystallization will expel further carbon dioxide. So as the dyke intruded upwards and decompressed, it would have naturally released carbon dioxide, with a steady flow of volatiles continuing as the melt solidified over subsequent months and years (Turner *et al.* 2012). This could explain both the initial months-long delay in shallow seismicity as the carbon dioxide moved upwards, and then the continuing shallow seismicity thereafter as volatiles continued to be fed by the crystallizing magma.

The carbon dioxide concentrations measured in mantle plume basalts from the Azores and Hawaii reach 800–1000 ppm (Kingsley & Schilling 1995; Hauri 2002). However, it is difficult to constrain original concentrations in the melt because volatiles may be lost before the magma freezes, so these may be unreliable measurements of the original concentrations. One approach to get round this problem is to examine presumed undegassed melt inclusions from oceanic basalt samples extruded under high pressure in deep water and to measure the CO<sub>2</sub>/Nb ratio in those inclusions: for samples from the Siqueros Fracture Zone, the CO<sub>2</sub>/Nb ratio is 239 ± 46 (Saal *et al.* 2002). If this same CO<sub>2</sub>/Nb ratio also applies to the Icelandic basalts, then the concentration of Nb, which is retained in extruded basalts, can be used to estimate the original CO<sub>2</sub> concentrations, even if degassing of the samples has led to the loss of CO<sub>2</sub>. Concentrations of Nb from basalts erupted in Herdubreid, the biggest Holocene eruption in Kollottadyngja, and the 20th century eruption of Askja, all of which are close to Upptyppingar, are >5, 10 and ~20 ppm, respectively (MacLennan *et al.* 2001; Kokfelt *et al.* 2006). From these, we infer original CO<sub>2</sub> contents of >1200, 2400 and ~4800 ppm, respectively in those melts. These concentrations

would cause saturation in CO<sub>2</sub> fluid, and exsolution of CO<sub>2</sub> at pressures of 5–7 kbar (15–20 km depth), just the depths at which the Upptyppingar intrusions occurred.

We use simple dimensional analysis to estimate a hydraulic diffusivity for the percolation of the volatiles through the mid-crust. Assuming a length scale,  $L$ , of 6.5 km and maximum and minimum time periods,  $t$ , of 14 and 5 months, respectively, we compute hydraulic diffusivities,  $D = L^2/t$ , of 1.0–3.3 m<sup>2</sup> s<sup>-1</sup>. The two time periods correspond to the time delays between the start and end of the intrusion and the onset of the shallow seismicity. The length scale represents the spatial separation between the shallowest extent of the dyke and the deepest extent of the shallow seismicity. Our range of hydraulic diffusivity is consistent with other seismic-based studies of crustal permeability and is sufficiently high to imply fluid flow along pre-existing fractures rather than diffusion through intact rock (Simpson *et al.* 1988; Shapiro *et al.* 1997; Waite & Smith 2002).

Shallow microearthquakes updip of the Upptyppingar intrusion continued at least through the end of 2012, but decreased in frequency. We recorded only 126 shallow events in our study area (black box in Fig. 1) over the entire year of 2012, compared to 178 in 2011, 469 in 2010 and 728 in 2009. The reducing level of activity with time following the intrusion is consistent with both depletion of the carbon dioxide source at depth following the termination of the magmatic intrusion in 2008 as well as having triggered many of the faults that were already primed and close to failure.

## CONCLUSIONS

The 2007 dyke intrusion beneath Mount Upptyppingar modified the local stress field across a region tens of kilometres in extent. Areas updip and overhead of the dyke exhibited positive changes in Coulomb stress for right-lateral strike-slip and normal receiver faults aligned with regional fractures, suggesting that the expansion of the dyke brought these areas closer to failure. The small set of cluster A events, directly above the dyke, might have been triggered outright due to this elastic stress change. Cluster B and C events updip of the dyke, in contrast, were triggered after a significant time delay of several months. We propose that the updip events in cluster B and possibly in cluster C were triggered by the release of carbon dioxide from magma within the dyke. The shallowest events (cluster C) were too distant to be influenced meaningfully by stress changes related to the dyke expansion and hence failed in the same sense as regional shallow seismicity and along faults orientated in the same direction. Updip events at the brittle–ductile boundary (cluster B), however, lie within a lobe of significant positive Coulomb stress change imposed by the dyke of up to 200 kPa (2.0 bar). The cluster B events failed in a right-lateral sense with fault planes aligned with the rift zone, suggesting that the earthquakes used pre-existing fabric. The right-lateral sense of motion, however, is opposite that of the regional transfer faults, but consistent with stresses imposed by the inflating dyke. The mean  $T$ -axis direction for cluster B aligns well with the dip and opening direction of the dyke. We therefore suggest that an injection of carbon dioxide, exsolved at much greater depths as the magma in the dyke decompressed and then crystallized, triggered the seismicity observed in cluster B and possibly cluster C by reducing the effective normal compressive stress on pre-existing faults, and that those events in cluster B failed in a direction consistent with local stress changes created by the dyke intrusion.

We note that the mechanism we have identified here of bringing faults to failure and triggering microearthquakes at very low applied stress levels as a result of the insertion of carbon dioxide may have wider applicability to discussions of the likelihood of inducing seismicity above regions of carbon dioxide sequestration or above regions where large quantities of fluids have been injected for hydrofracture.

## ACKNOWLEDGEMENTS

Seismometers were borrowed from the Natural Environment Research Council SEIS-UK (loans 842 and 914). We thank Heidi Soosalu, Janet Key and all those who have assisted in fieldwork in Iceland since 2007. We are grateful to Ásta Hjartardóttir and Páll Einarsson for providing raw data on fracture orientations from the Upptyppingar region and to Rob Green for providing epicentral locations from his work on earthquakes on strike-slip faults between the Askja and Kverkfjöll segments. We thank Marie Edmonds and John MacLennan for giving valuable advice on carbon dioxide concentrations and degassing in Icelandic lavas. We acknowledge Alex Copley and Nadia Lapusta for providing helpful comments on the modelling portion of this manuscript and thank Brad Aagaard and Charles Williams for training and support in using *PyLith*. We also appreciate the helpful suggestions made by two anonymous reviewers to strengthen the manuscript. The IMO kindly provided data from their seismometers in northeast Iceland. This manuscript is based upon work supported by the National Science Foundation Graduate Research Fellowship to HRM under Grant No. DGE-1144469. Department of Earth Sciences, Cambridge contribution number ESC2755.

## REFERENCES

- Aagaard, B., Williams, C. & Knepley, M., 2008. PyLith: a finite-element code for modeling quasi-static and dynamic crustal deformation, *EOS, Trans. Am. Geophys. Un.*, **89**(53), Fall Meet. Suppl., Abstract T41A-1925.
- Arnadóttir, T., Lund, B., Jiang, W., Geirsson, H., Björnsson, H., Einarsson, P. & Sigurdsson, T., 2009. Glacial rebound and plate spreading: results from the first countrywide GPS observations in Iceland, *Geophys. J. Int.*, **177**, 691–716.
- Böðvarsson, R., Rögnvaldsson, S.T., Slunga, R. & Kjartansson, E., 1999. The SIL data acquisition system—at present and beyond year 2000, *Phys. Earth planet. Inter.*, **113**, 89–101.
- Chiodini, G., Cardellini, C., Amato, A., Boschi, E., Caliro, S., Frondini, F. & Ventura, G., 2004. Carbon dioxide Earth degassing and seismogenesis in central and southern Italy, *Geophys. Res. Lett.*, **31**, L07615, doi:10.1029/2004GL019480.
- Darbyshire, F.A., White, R.S. & Priestly, K.F., 2000. Structure of the crust and uppermost mantle of Iceland from a combined seismic and gravity study, *Earth planet. Sci. Lett.*, **181**, 409–428.
- DeMets, C., Gordon, R.G., Argus, D.F. & Stein, S., 1994. Effect of recent revisions to the geomagnetic reversal time scale on estimates of current plate motions, *Geophys. Res. Lett.*, **21**, 2191–2194.
- Drew, J., 2010. Coalescence microseismic mapping: an imaging method for the detection and location of seismic events, *PhD thesis*, University of Cambridge, 224pp.
- Einarsson, P., 1991. Earthquakes and present-day tectonism in Iceland, *Tectonophysics*, **189**, 261–279.
- Fournier, R.O., 1999. Hydrothermal processes related to movement of fluid from plastic into brittle rock in the magmatic-epithermal environment, *Econ. Geol.*, **94**, 1193–1211.
- Freed, A.M., 2005. Earthquake triggering by static, dynamic, and postseismic stress transfer, *Annu. Rev. Earth planet. Sci.*, **33**, 335–367.

- Grasso, J.-R., 1992. Mechanics of seismic instabilities induced by the recovery of hydrocarbons, *Pure appl. Geophys.*, **139**(3–4), 507–534.
- Green, R.G., 2012. Swarm microseismicity and upper crustal faulting between the Askja and Kverkfjöll volcanic systems, Iceland, *MSci thesis*, University of Cambridge.
- Hainzl, S., 2004. Seismicity patterns of earthquake swarms due to fluid intrusion and stress triggering, *Geophys. J. Int.*, **159**, 1090–1096.
- Harris, R.A., 1998. Introduction to special section: stress triggers, stress shadows, and implications for seismic hazard, *J. geophys. Res.*, **103**(B10), 24 347–24 358.
- Harris, R.A., Simpson, R.W. & Reasenber, P.A., 1995. Influence of static stress changes on earthquake locations in southern California, *Nature*, **375**, 221–224.
- Hauri, E., 2002. SIMS analysis of volatiles in silicate glasses, 2: isotopes and abundances in Hawaiian melt inclusions, *Chem. Geol.*, **183**, 115–141.
- Hjartardóttir, Á.R. & Einarsson, P., 2012. The Kverkfjöll fissure swarm and the eastern boundary of the Northern Volcanic Rift Zone, Iceland, *Bull. Volcanol.*, **74**, 143–162.
- Hooper, A., Ófeigsson, B., Sigmundsson, F., Lund, B., Einarsson, P., Geirsson, H. & Sturkell, E., 2011. Increased capture of magma in the crust promoted by ice-cap retreat in Iceland, *Nature Geosci.*, **4**, 783–786.
- Jakobsdóttir, S.S., Roberts, M.J., Guðmundsson, G.B., Geirsson, H. & Slunga, R., 2008. Earthquake swarms at Upptyppingar, north-east Iceland: a sign of magma intrusion? *Stud. Geophys. Geod.*, **52**, 513–528.
- Jull, M. & McKenzie, D., 1996. The effect of deglaciation on mantle melting beneath Iceland, *J. geophys. Res.*, **101**(B10), 21 815–21 828.
- Key, J., White, R.S., Soosalu, H. & Jakobsdóttir, S.S., 2011a. Multiple melt injection along a spreading segment at Askja, Iceland, *Geophys. Res. Lett.*, **38**, L05301, doi:10.1029/2010GL046264.
- Key, J., White, R.S., Soosalu, H. & Jakobsdóttir, S.S. 2011b. Correction to ‘Multiple melt injection along a spreading segment at Askja, Iceland’, *Geophys. Res. Lett.*, **38**, L10308, doi:10.1029/2011GL047491.
- King, C.P., Stein, R.S. & Lin, J., 1994. Static stress changes and the triggering of earthquakes, *Bull. seism. Soc. Am.*, **84**(3), 935–953.
- Kingsley, R.H. & Schilling, J.-G., 1995. Carbon in Mid-Atlantic Ridge basalt glasses from 28°N to 63°N: evidence for a carbon-enriched Azores mantle plume, *Earth planet. Sci. Lett.*, **129**, 31–53.
- Kissling, E., Ellsworth, W.L., Eberhart-Phillips, D. & Kradolfer, U., 1994. Initial reference models in local earthquake tomography, *J. geophys. Res.*, **99**(B10), 19 635–19 646.
- Kisslinger, C., 1976. A review of theories of mechanisms of induced seismicity, *Eng. Geol.*, **10**, 85–98.
- Klein, F.W., 2002. User’s guide to Hypoinverse-2000, a FORTRAN program to solve for earthquake locations and magnitudes, Open File Report 02-171, USGS.
- Kokfelt, T.F., Hoernle, K.A.J., Hauff, F., Fiebig, J., Werner, R. & Garbe-Schonberg, D., 2006. Combined trace element and Pb-Nd-Sr-O isotope evidence for recycled oceanic crust (upper and lower) in the Iceland mantle plume, *J. Petrol.*, **47**, 1705–1749.
- Lindenfeld, M., Rumpker, G., Link, K., Koehn, D. & Batte, A., 2012. Fluid-triggered earthquake swarms in the Rwenzori region, East African Rift—evidence for rift initiation, *Tectonophysics*, **566–567**, 95–104.
- Lowenstern, J.B., 2001. Carbon dioxide in magmas and implications for hydrothermal systems, *Miner Deposita*, **26**, 490–502.
- Maccaferri, F., Bonafede, M. & Rivalta, E., 2010. A numerical model of dyke propagation in layered elastic media, *Geophys. J. Int.*, **180**, 1107–1123.
- MacLennan, J., McKenzie, D., Gronvöld, K. & Slater, L., 2001. Crustal accretion under northern Iceland, *Earth planet. Sci. Lett.*, **191**, 295–310.
- Martens, H.R., 2010. Microseismic evidence for active dyke emplacement in Iceland’s Northern Volcanic Zone, *MPhil thesis*, University of Cambridge.
- Martens, H.R., White, R.S., Key, J., Drew, J., Soosalu, H. & Jakobsdóttir, S.S., 2010. Dense seismic network provides new insight into the 2007 Upptyppingar dyke intrusion, *Jökull*, **60**, 47–66.
- Miller, S.A., Colletini, C., Chiaraluce, L., Cocco, M., Barchi, M. & Kaus, J.P., 2004. Aftershocks driven by a high-pressure CO<sub>2</sub> source at depth, *Nature*, **427**, 724–727.
- Pan, V., Holloway, J.R. & Hervig, R.L., 1991. The pressure and temperature dependence of carbon dioxide solubility in tholeiitic basalt melts, *Geochem. Cosmochim. Acta*, **55**, 1587–1595.
- Plateaux, R., Bergerat, F., Béthoux, N., Villemin, T. & Gerbault, M., 2012. Implications of fracturing mechanisms and fluid pressure on earthquakes and fault slip data in the east Iceland rift zone, *Tectonophysics*, **581**, 19–34.
- Pollitz, F.F. & Sacks, I.S., 1996. Viscosity structure beneath northeast Iceland, *J. geophys. Res.*, **101**(B8), 17 771–17 793.
- Reasenber, P.A. & Oppenheimer, D., 1985. FPFIT, FPLOT and FPPAGE: Fortran computer programs for calculating and displaying earthquake fault—plane solutions, Open File Report 85-739, USGS.
- Reasenber, P.A. & Simpson, R.W., 1992. Response of regional seismicity to the static stress change produced by the Loma Prieta earthquake, *Science*, **255**, 1687–1690.
- Reyners, M., Eberhart-Phillips, D. & Stuart, G., 2007. The role of fluids in lower-crustal earthquakes near continental rifts, *Nature*, **446**, 1075–1078.
- Rother, E. & Shapiro, S.A., 2007. Statistics of fracture strength and fluid-induced microseismicity, *J. geophys. Res.*, **112**, B04309, doi:10.1029/2005JB003959.
- Saal, A.E., Hauri, E.H., Langmuir, C.H. & Perfit, M.R., 2002. Vapour undersaturation in primitive mid-ocean-ridge basalt and the volatile content of Earth’s upper mantle, *Nature*, **419**, 451–455.
- Shapiro, S.A., Huenges, E. & Borm, G., 1997. Estimating the crust permeability from fluid-injection-induced seismic emission at the KTB site, *Geophys. J. Int.*, **131**, F15–F18.
- von Seggern, D.H., Smith, K.D. & Preston, L.A., 2008. Seismic spatial-temporal character and effects of a deep (25–30 km) magma intrusion below north Lake Tahoe, California-Nevada, *Bull. seism. Soc. Am.*, **98**(3), 1508–1526.
- Shelly, D.R. & Hill, D.P., 2011. Migrating swarms of brittle-failure earthquakes in the lower crust beneath Mammoth Mountain, California, *Geophys. Res. Lett.*, **38**, L20307, doi:10.1029/2011GL049336.
- Simpson, D.W., Leith, W.S. & Scholz, C.H., 1988. Two types of reservoir-induced seismicity, *Bull. seism. Soc. Am.*, **78**(6), 2025–2040.
- Smith, K.D., von Seggern, D., Blewitt, G., Preston, L., Anderson, J.G., Wernicke, B.P. & Davis, J.L., 2004. Evidence for deep magma injection beneath Lake Tahoe, Nevada-California, *Science*, **305**, 1277–1280.
- Soosalu, H., Key, A.J., White, R.S., Knox, C., Einarsson, P. & Jakobsdóttir, S.S., 2010. Lower-crustal earthquakes caused by magma movement beneath Askja volcano on the north Iceland rift, *Bull. Volcanol.*, **72**, 55–62.
- Stacy, S., Gombert, J. & Cocco, M., 2005. Introduction to special section: stress transfer, earthquake triggering, and time-dependent seismic hazard, *J. geophys. Res.*, **110**, B05S01, doi:10.1029/2005JB003692.
- Stein, R.S., King, G.C.P. & Lin, J., 1994. Stress triggering of the 1994 M = 6.7 Northridge, California, earthquake by its predecessors, *Science*, **265**, 1432–1435.
- Stein, R.S., Barka, A.A. & Dieterich, J.H., 1997. Progressive failure on the North Anatolian fault since 1939 by earthquake stress triggering, *Geophys. J. Int.*, **128**(3), 594–604.
- Tarasiewicz, J., White, R.S., Brandsdóttir, B. & Thorbjarnardóttir, B., 2011. Location accuracy of earthquake hypocentres beneath Eyjafjallajökull, Iceland, prior to the 2010 eruptions, *Jökull*, **61**, 33–50.
- Tarasiewicz, J., Brandsdóttir, B., White, R.S., Hensch, M. & Thorbjarnardóttir, B., 2012. Using microearthquakes to track repeated magma intrusions beneath the Eyjafjallajökull stratovolcano, Iceland, *J. geophys. Res.*, **117**, B00C06, doi:10.1029/2011JB008751.
- Toda, S., Stein, R.S., Richards-Dinger, K. & Bozkurt, S., 2005. Forecasting the evolution of seismicity in southern California: animations built on earthquake stress transfer, *J. geophys. Res.*, **110**, B05S16, doi:10.1029/2004JB003415.
- Turner, S., Reagan, M., Vigier, N. & Bourdon, B., 2012. Origins of <sup>210</sup>Pb–<sup>226</sup>Ra disequilibria in basalts: new insights from the 1978 Asal Rift eruption, *Geochem. Geophys. Geosyst.*, **13**, doi:10.1029/2012GC004173.
- Van Eijs, R.M.H.E., Mulders, F.M.M., Nepveu, M., Kenter, C.J. & Scheffers, B.C., 2006. Correlation between hydrocarbon reservoir properties and induced seismicity in the Netherlands, *Eng. Geol.*, **84**(3–4), 99–111.



- Waite, G.P. & Smith, R.B., 2002. Seismic evidence for fluid migration accompanying subsidence of the Yellowstone caldera, *J. geophys. Res.*, **107**(B9), 2177, doi:10.1029/2001JB000586.
- Waldhauser, F., 2001. HypoDD: a computer program to compute double-difference hypocenter locations, Open File Report 01-113, USGS.
- Waldhauser, F. & Ellsworth, W.L., 2000. A double-difference earthquake location algorithm: method and application to the Northern Hayward Fault, California, *Bull. seism. Soc. Am.*, **90**(6), 1353–1368.
- White, R.S., Drew, J., Martens, H.R., Key, A.J., Soosalu, H. & Jakobsdóttir, S.S., 2011. Dynamics of dyke intrusion in the mid-crust of Iceland, *Earth planet. Sci. Lett.*, **304**, 300–312.
- Williams, C.A., Aagaard, B. & Knepley, M.G., 2005. Development of software for studying earthquakes across multiple spatial and temporal scales by coupling quasi-static and dynamic simulations, *EOS, Trans. Am. geophys. Un.*, **86**(52), Fall Meet. Suppl., Abstract S53A-1072.
- Ziv, A. & Rubin, A.M., 2000. Static stress transfer and earthquake triggering: no lower threshold in sight? *J. geophys. Res.*, **105**(B6), 13 631–13 642.

## SUPPORTING INFORMATION

Additional Supporting Information may be found in the online version of this article:

- Figure S1.** Synthetic tests for accuracy of hypocentre depth recovery after location using HypoInverse-2000 (Klein 2002).
- Figure S2.** Local magnitudes determined by the Icelandic Meteorological Office as a function of occurrence time for microseismic events in the reduced CMM catalogue (see main text for a description of the catalogue).
- Figure S3.** Fault plane solutions output by FPFIT for all manually located events in (a) cluster A directly overhead of the dyke, (b) cluster B at the brittle–ductile boundary and (c) cluster C at depths near to the surface.

**Figure S4.** Coulomb stress change patterns for a typical event in cluster A (left-hand panels), but assuming slip on the alternative nodal plane (204/25/−90) to that considered in Fig. 10 from the main text, as well as Coulomb stress change patterns on strike-slip receiver faults aligned with the rift fabric (right-hand panels), such as those of cluster B, but assuming left-lateral slip (23/90/000).

**Table S1.** List of seismic stations active during separate portions of our study period (2007–2011).

**Table S2.** Values of seismic wave velocity and density with depth, used for hypocentre location and finite-element modelling.

**Table S3.** Spatial database file used to impose initial displacements on the modelled dyke.

**Table S4.** Observed and predicted surface displacements at the locations of seven GPS stations near to Mount Uppþýppingar over the course of the dyke intrusion in the mid-crust.

**Movie S1.** The migration of microseismic hypocentres (determined from manually refined time picks and double-difference relocation) along the dip direction of the inferred dyke plane and looking along strike.

**Movie S2.** The migration of microseismic hypocentres along the strike direction of the inferred dyke plane (74°).

**Movie S3.** The migration of epicentres from the shallow cluster C through time.

(<http://gji.oxfordjournals.org/lookup/suppl/doi:10.1093/gji/ggt184/-/DC1>)

Please note: Oxford University Press is not responsible for the content or functionality of any supporting materials supplied by the authors. Any queries (other than missing material) should be directed to the corresponding author for the article.